Electronic Supplementary Material (ESI) for ChemComm.

Supporting Information

Ionic Ultramicroporous Polymer with Engineered Nanopores Enable Enhanced Acetylene/Carbon Dioxide Separation

Asif Raza,[a,†] Sousa Javan Nikkhah,[a,†] Lilia Croitor,[a] Ahmed Gamal Attallah,[b] Eric Hirschmann,[b] Matthias Vandichel,[*a] and Soumya Mukherjee[*a]

[a] *Department of Chemical Sciences, Bernal Institute and Research Ireland Centre for Pharmaceuticals (SSPC), University of Limerick, Limerick V94 T9PX, Ireland. E-mails: Matthias.Vandichel@ul.ie; Soumya.Mukherjee@ul.ie*

[b] *Helmholtz-Zentrum Dresden - Rossendorf, Institute of Radiation Physics, Bautzner Landstraße 400, 01328, Dresden, Germany.*

[†] *A.R. and S.J.N. contributed equally.*

Contents

Methods.

Materials and general experimental procedures

All chemicals were used without further purification. 1-vinylimidazole (99%) was purchased from Fluorochem. 1,3,5-tris(bromomethyl)benzene (>98%) was purchased from TCI. 2,6-di-tert-butyl-4-methylphenol (BHT, 99%) and 2,2'-azobis(2-methylpropionitrile) (AIBN, 99%, Solution 0.2M in toluene) were purchased from Sigma Aldrich. Solvents such as Ethanol (EtOH), acetonitrile (CH_3CN) and ethyl acetate (EA) were of analytical grade (purchase from Sigma Aldrich).

All the gases, including CO_2 (99.999%), N_2 (99.9992%), helium (99.996%) and acetylene (99.9995%) were purchased from BOC Gases Ireland. Each was used directly without further purification.

Synthesis of 1-(4-vinylbenzyl)-1H-imidazole

This was synthesized using a modified procedure reported in literature.[1] Sodium bicarbonate (16.05 mmol, 1.3125 g) and imidazole (0.04975 mmol, 3.4025 g) were added in round bottom flask along with 12.mL deionized water and 12.5mL acetone, the mixture was sonicated for 5 minutes a white dispersion was obtained. This mixture was refluxed at 50 °C for 30 minutes under nitrogen atmosphere. After it was cooled down to room temperature, 1-(chloromethyl)-4-vinylbenzene (12.45 mmol, 1.756 mL) dropwise. Then this mix was refluxed at 50 °C under nitrogen for overnight. The next day, crude was filtered, acetone was removed by rotary evaporator, then extracted with diethyl ether (50 mL, three times), the organic phase was collected, this was further washed twice with 2.0 M hydrochloric acid, and the aqueous phase was collected. This was added in 4.0 M sodium hydroxide solution and was extracted with diethyl ether (50 mL, 4 times), organic phase was collected and dried with $MgSO_4$. This was concentrated using a rotary evaporator, leading to yellow oil (25% yield). This was further characterized by ^{1}H NMR (Fig. S1).

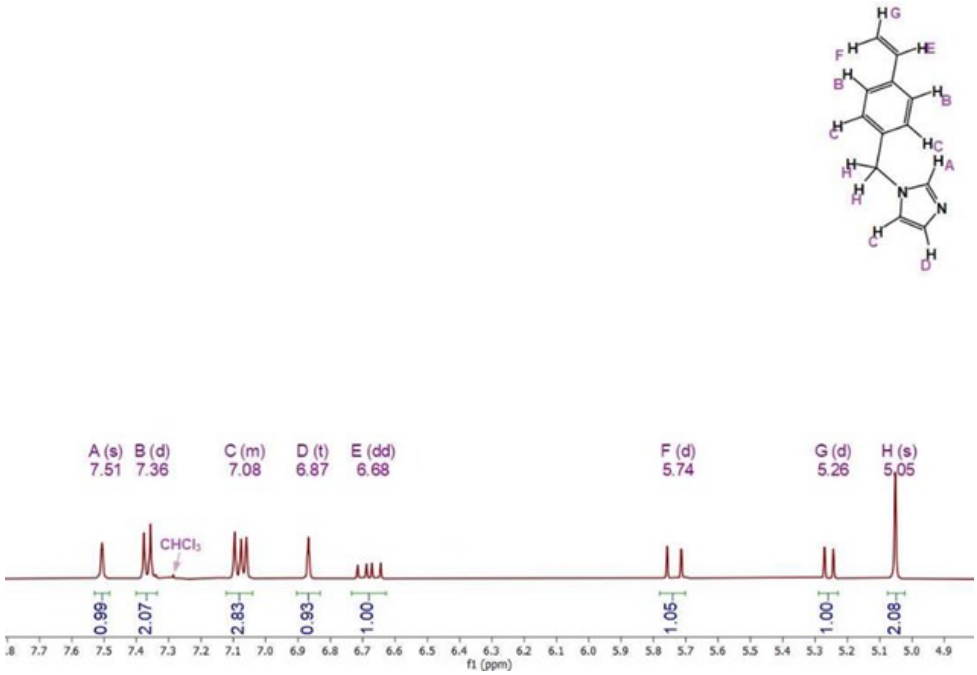

Figure S1: ^{1}H NMR spectrum of 1-(4-vinylbenzyl)-1*H*-imidazole recorded in $CDCl_3$.

Synthesis of ionic monomers.

In a thick glass pressure vessel, 1,3,5-tris(bromomethyl)benzene (471.08 mg, 1.32 mmol), and BHT (23.7 mg, 0.1 mmol) were dissolved in CH_3CN (15 mL). This mixture was heated to 65 °C and then a slight excess of 1-vinylimidazole (388µL, 4.32 mmol) or 1-(4-vinylbenzyl)-1*H*-imidazole (0.88mL, 5mmol) was added, after 10 minutes a white precipitate appeared whereafter the mixture was left under heating 65 °C for 18 hours. After cooling to room temperature, the precipitate was filtered and washed with CH_3CN and was further purified by Soxhlet extraction using CH_3CN for 8 hours. Then the powder was dried at 80 °C under reduced pressure. The products were characterized by ^{1}H NMR.

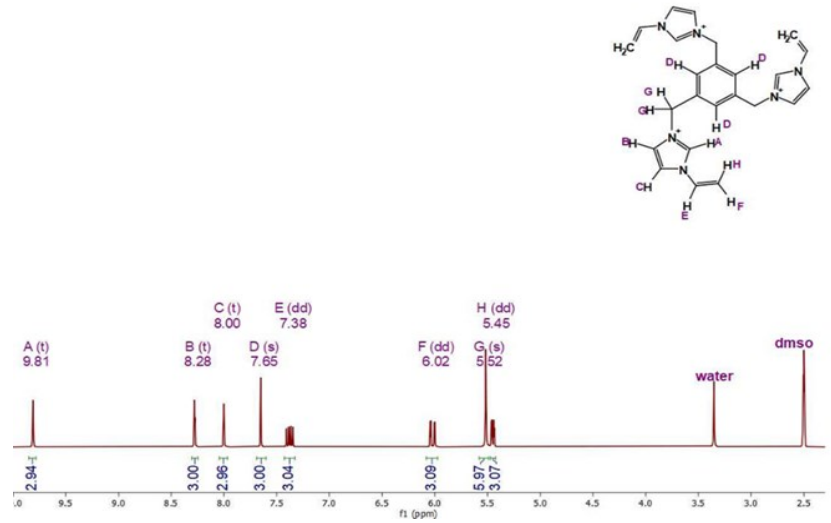

Figure S2: ^{1}H NMR spectrum of **Ph3MVIm-Br** in DMSO-d_6 solvent.

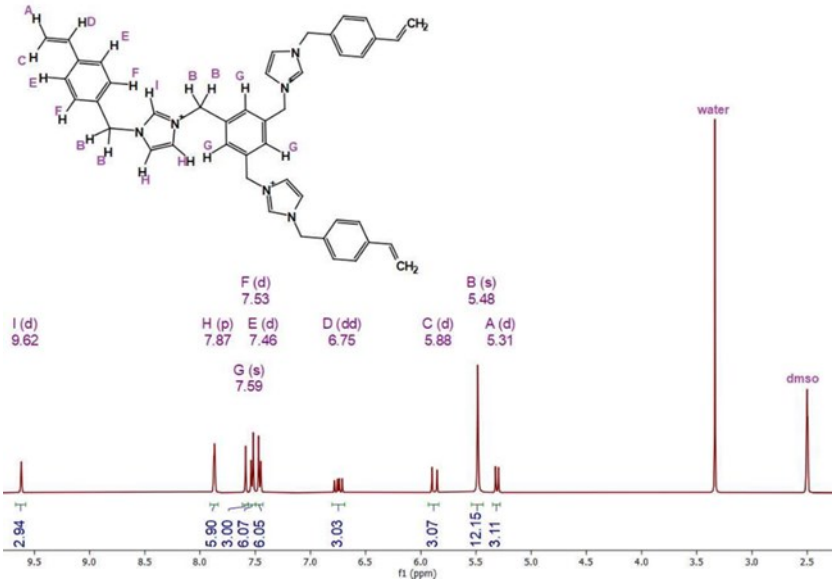

Figure S3: ^{1}H NMR spectrum for **Ph3MVIBm-Br** in DMSO-d_6 solvent.

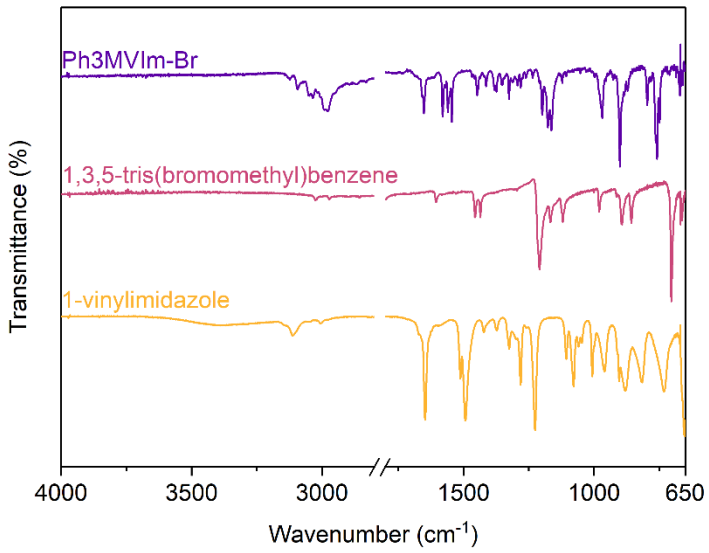

Figure S4: FTIR spectra of **Ph3MVIm-Br** (purple line), along with the starting materials.

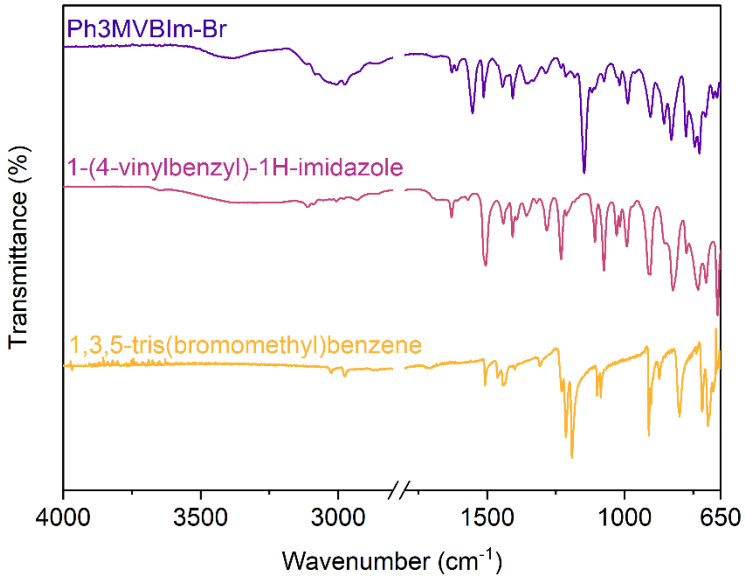

Figure S5: FTIR spectra of **Ph3MVBIm-Br** (purple line), along with the starting materials.

Synthesis of ionic polymers derived from ionic monomers with different branched structures.

The ionic polymers were synthesized via free-radical polymerization technique. In ~50 mL volume Schlenk flask 1.25 mmol of monomer was charged along with 5 mL ethanol and 1.25 mL deionized water. 900 µL of AIBN solution was also added. Subsequently, the above solution was deoxygenated three times by free-pump-thaw procedure and backfilled with nitrogen. Then it was stirred vigorously at room temperature for two hours followed by heating at 80 °C for 24 hours. After cooling to room temperature, the sample was thoroughly washed with water and was subjected to further purification by Soxhlet extraction under methanol for next 18 hours. The products were dried at 80 °C under reduced pressure till it reached a constant weight.

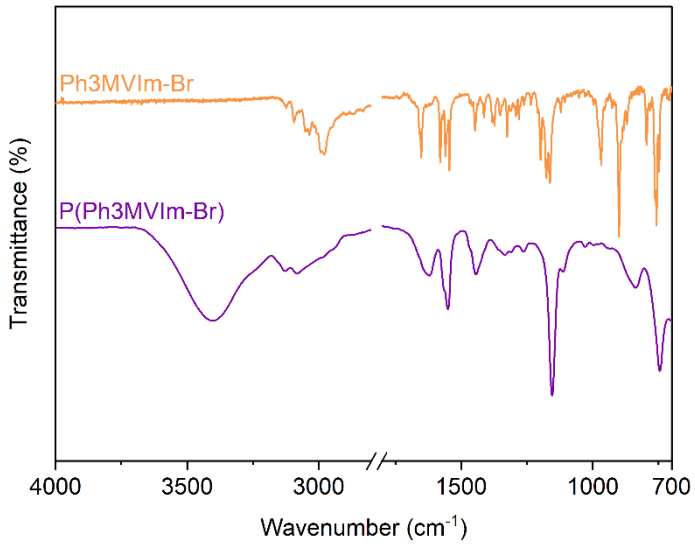

Figure S6: FTIR spectra of the polymer **P(Ph3MVIm-Br)** (purple line), along with the monomer.

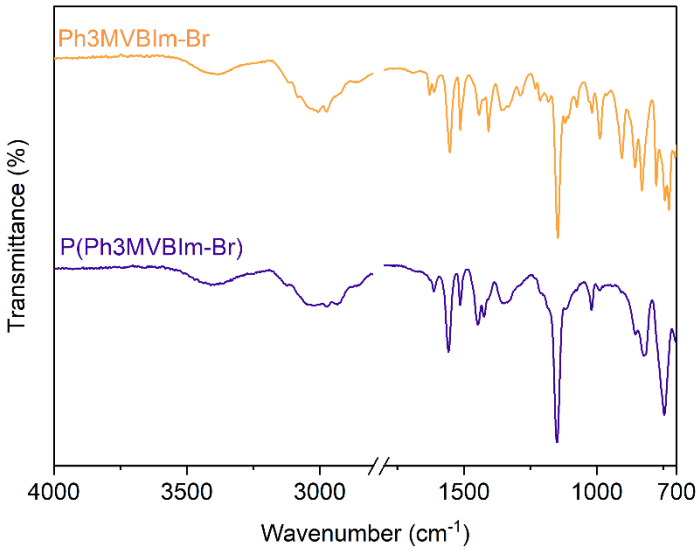

Figure S7: FTIR spectra of the polymer **P(Ph3MVBIm-Br)** (purple line), along with the monomer.

Single-component gas sorption experiments.

The methanol exchanged polymers were activated under high vacuum by a Micromeritics® Smart VacPrep™ at 80 °C for 12 h before gas sorption studies. The CO_2 sorption isotherms at 195 K were measured by a Micromeritics® 3Flex adsorption analyser. The 195 K environment was controlled by a 2.75 L dewar vessel containing a bath of acetone and dry ice. 273 K, 283 K and 298 K environment was controlled by a Julabo temperature controller with the ethylene glycol/water = 1:1 (v/v) mixture liquid. Surface areas were calculated from the adsorption data using Langmuir method. The pore-size-distribution curves were obtained from the adsorption branches using Horvath-Kawazoe (H-K) method.

Table S1: Textural properties and structural parameters derived from the CO_2 isotherms at 195 K.

Sample	$S_{Langmuir}$ [m^2/g]	CO_2 uptake at 1 bar [mmol/g]	Horvath Kawazoe pore width range [Å]
P(Ph3MVIm-Br)	212.2	2.02	4 – 10
P(Ph3MVBIm-Br)	238.8	2.27	3.8 –10

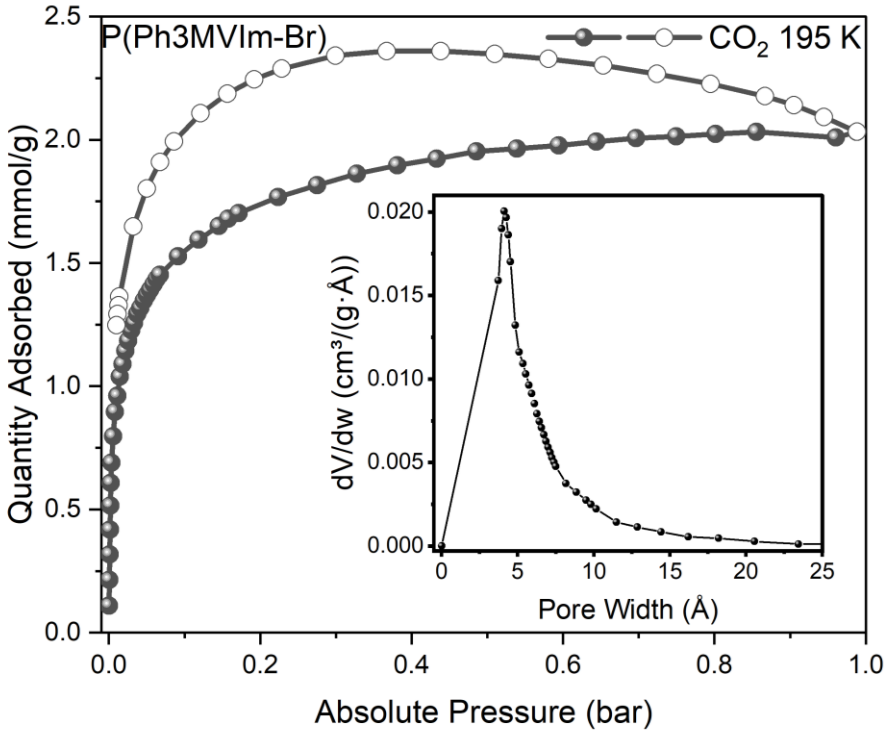

Figure S8: CO_2 sorption isotherm recorded at 195 K for **P(Ph3MVIm-Br)**; pore size distribution plot using Horvath-Kawazoe model (inset). Closed and open symbols denote adsorption and desorption, respectively.

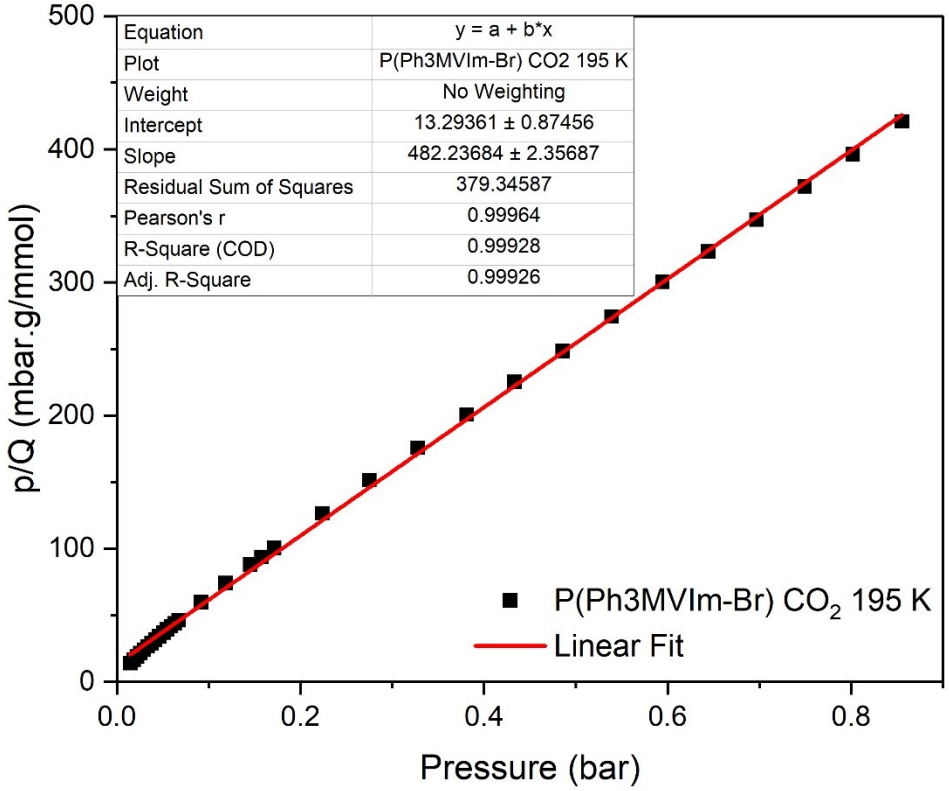

Figure S9: Langmuir surface area plot for **P(Ph3MVIm-Br)** obtained from CO_2 adsorption isotherm recorded at 195 K.

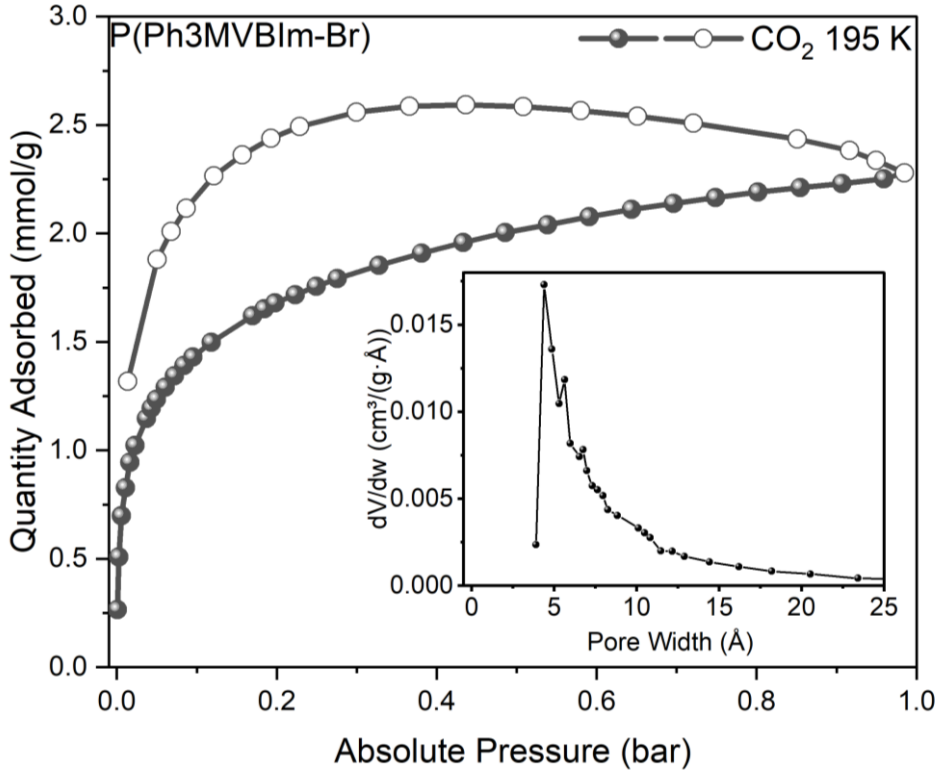

Figure S10: CO_2 sorption isotherm recorded at 195 K for **P(Ph3MVBIm-Br)**; pore size distribution plot using Horvath-Kawazoe model (inset). Closed and open symbols denote adsorption and desorption, respectively.

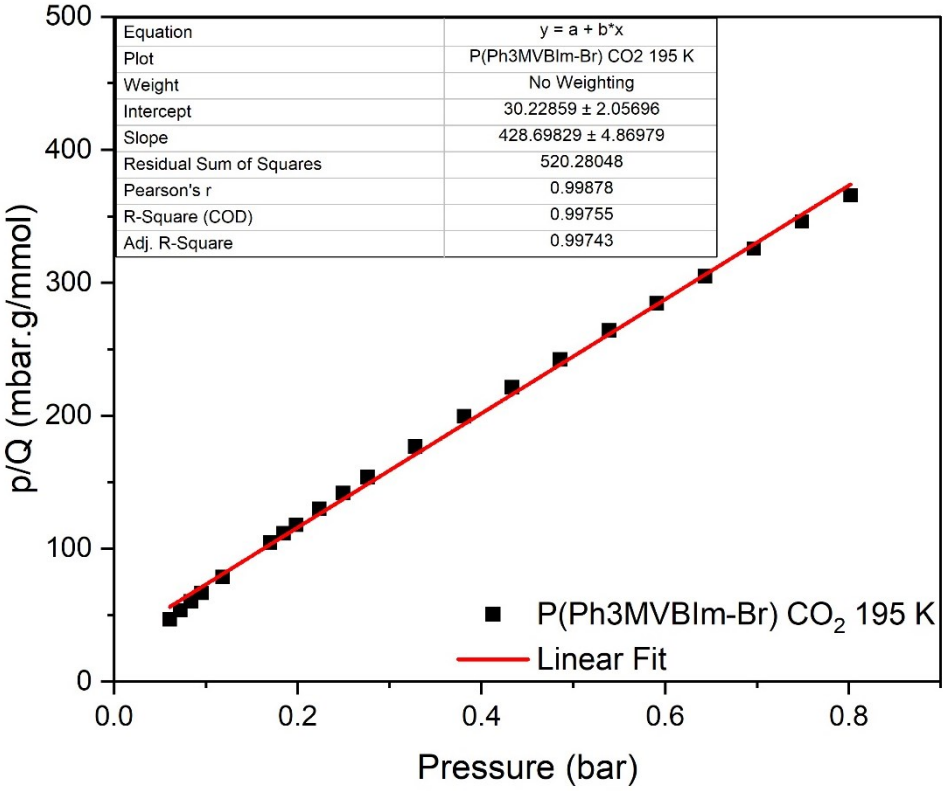

Figure S11: Langmuir surface area plot for **P(Ph3MVBIm-Br)** obtained from CO_2 adsorption isotherm recorded at 195 K.

Positron annihilation lifetime spectroscopy (PALS).

Basics. Positrons emitted from ^{22}Na have endpoint energies of up to 540 keV and need to cool down (thermalization) before annihilation with an electron in the material. As result of this process, positrons are implanted up to 0.5 to 1 mm (depending on the materials density). After thermalization, the positron starts to diffuse and probes its environment.

Thermalized positrons are attracted to and trapped in open-volume defects, voids in material's matrix, interparticle spaces, and open and closed pores (because of the missing repelling nuclei).[2] In polymers and low free electron density materials, positrons can bind electrons with free space > ~2 Å ^{3} forming positronium (Ps). Ps has two states that depend on the spin alignment of electron and positron; para-positronium (*p*-Ps) and ortho-positronium (*o*-Ps). *p*-Ps is a singlet state with antiparallel spins and decays by two-511 keV photons with 0.125 ns lifetime in vacuum. However, *o*-Ps is a triplet state with parallel spins and decays by emitting 3 photons with intrinsic lifetime of 142 ns in vacuum. The short-lived *p*-Ps is weakly affected by the surrounding media,[4] hence it cannot be used for measuring the size of free volumes. The sufficiently long-lived *o*-Ps is capable of approaching the pore wall many times before annihilation and its lifetime is because of that reduced depending on the size of the probed free volumes. This process is known as *pick-off* annihilation.[5] The *pick-off* annihilation probability (reciprocal of *o*-Ps lifetime) is large for free volumes and decreases the *o*-Ps lifetime. This means that this collisionally-reduced *o*-Ps lifetime provides the physical basis for probing free volumes by PALS.[6] The correlation between o-Ps lifetime and pore size has been firstly described by the Tao-Eldrup (TE) model

[7,8] which is valid for spherical micropores (R < 1 nm). Later it was extended to include larger pores of different shapes and at different temperature.[5,9] Since in the current project PALS has been used to measure the free volume in polymeric protein, the TE model is suitable for correlating the Ps lifetimes to hole sizes. The relation between the measured o-Ps lifetime ($\boldsymbol{\tau_{o-Ps}}$) and hole radius (r_h) [7,8] is expressed as:

$$\boldsymbol{\tau_{o-Ps} = 0.5\ ns\ [1 - \frac{r_h}{r_h + \delta_r} + \frac{1}{2\pi}\sin(\frac{2\pi r_h}{r_h + \delta_r})]^{-1}} \qquad (1)$$

The 0.5 ns is the spin-averaged lifetime of the Ps, and the empirically determined δ_r) 1.66 Å describes the penetration of the Ps wave function into the hole "walls".

Assuming spherical open volume, the hole volume V_h can be calculated via:

$$\boldsymbol{V_h = \frac{4}{3}\pi\, r_h{}^3}. \qquad (2)$$

Experiments. PALS experiments were performed using a digitizer (Teledyne SP-Devices, ADQ14DC-2X-MTCA) with four photomultiplier tubes (Hamamatsu R13089, Model 265) coupled to cylindrical $CeBr_3$ scintillators (2-inch diameter 1 inch thickness) for the detection of gamma radiation associated with positron annihilation. Before PALS measurements on polymer, reference samples (Ta, Al) were used to determine the source contribution (*i.e.*, positrons annihilating in the source material) and instrument resolution function. These reference materials are characterized by a single positron lifetime component in addition to the source components, which leads to constant values of both resolution function and source correction. The source contribution was found to be 11 % of two components: 0.382 ns (97.98%) and 3.20 ns (2.2%). These two components considered and extracted from the actual sample analysis. Following that:

(i) the polymer samples have been measured under vacuum (~ 10^{-7} mbar) at RT to identify the free volume in the as-received samples.

(ii) consequently, samples were heated at 353 K for 2 h in order to remove any potential absorbed moisture in the free volumes of the polymer.

(iii) then, samples were scanned at different temperature from 353 K to 173 K with 10 K / step to check for any possible glass transitions in the polymers.

The PALSFit [10] code was used to analyze the spectra and three positron lifetime components have been obtained; (i) p-Ps (τ_1=0.150-0.180 ns), (ii) free (unbounded) positron (τ_2=0.41-0.43 ns, fixed at 0.42 ns), and (iii) *o*-Ps in free volumes (τ_3=1.7-2.2 ns). PALS results in free volumes (τ_3) of **P(Ph3MVIm-Br)** in brown and **P(Ph3MVBIm-Br)** samples as functions of temperatures are presented in **Fig. S12**. The pink data represent the results of the ac-received samples before activation at 353 K.

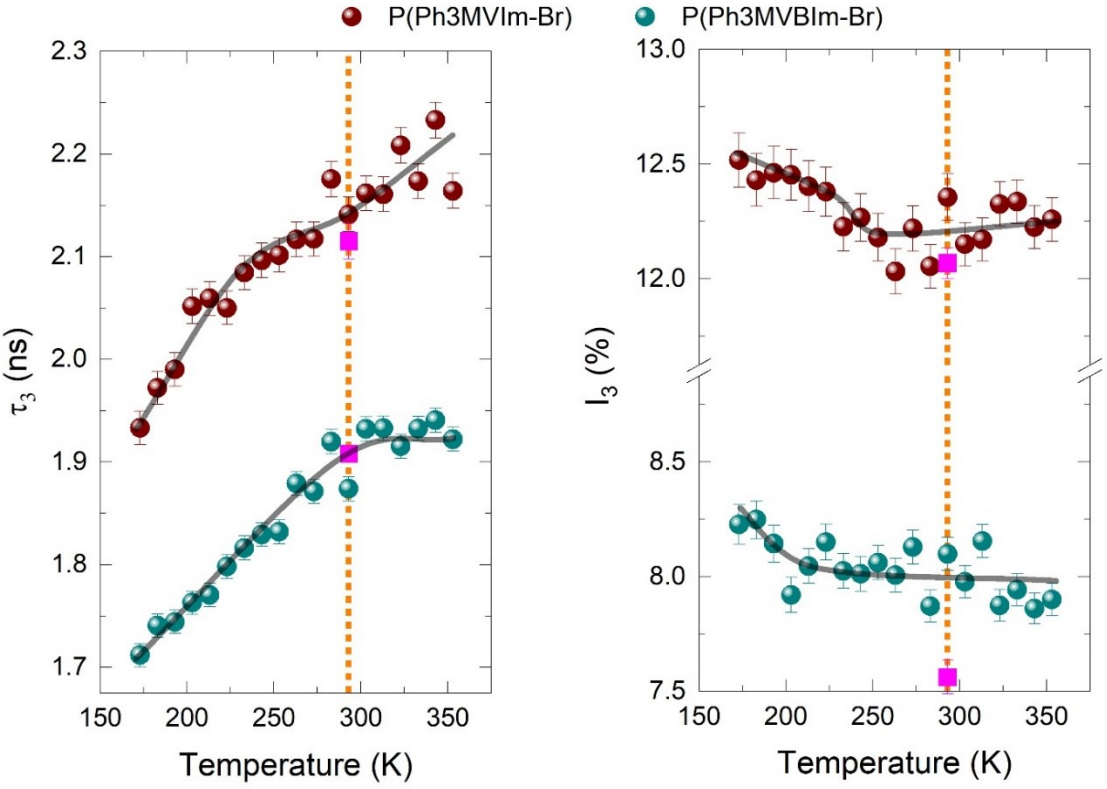

Figure S12: Dependence of o-Ps lifetime and intensity of the IUPs: **P(Ph3MVIm-Br)** in brown and **P(Ph3MVBIm-Br)** in green colour on temperature, orange line is to highlight room temperature, pink data is value before activation of the sample.

Thermogravimetric analysis (TGA).

Thermograms were recorded under nitrogen using TGA instrument TA Q50 V20.13 Build 39. Aluminium pans and a flow rate of 60 $cm^3\ min^{-1}$ for the nitrogen gas were used for the experiments. The data was collected in the High-Resolution Dynamic mode with a sensitivity of 1.0, a resolution of 4.0, and a temperature ramp of 10 $K\ min^{-1}$ up to 773 K. The data was evaluated using the T.A.

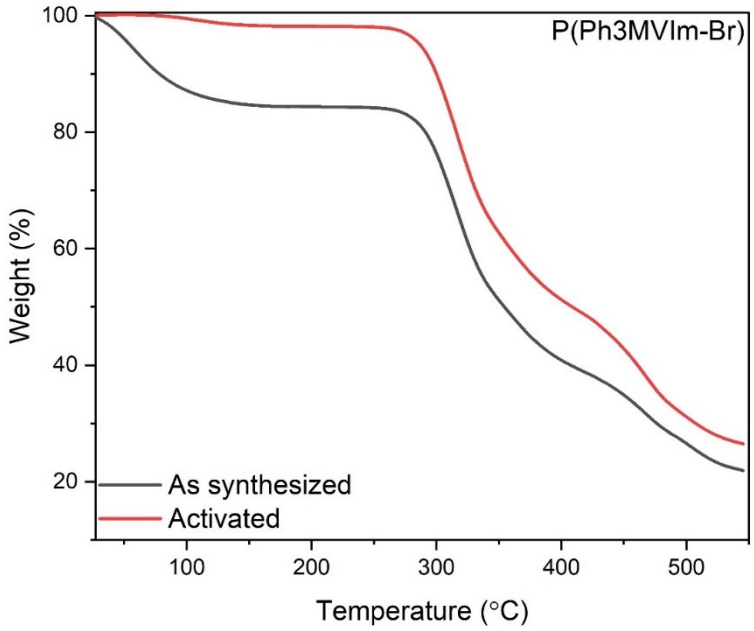

Figure S13: Thermogravimetric analysis profiles for polymer **P(Ph3MVIm-Br)** as-synthesized (in black) and activated phase (in red).

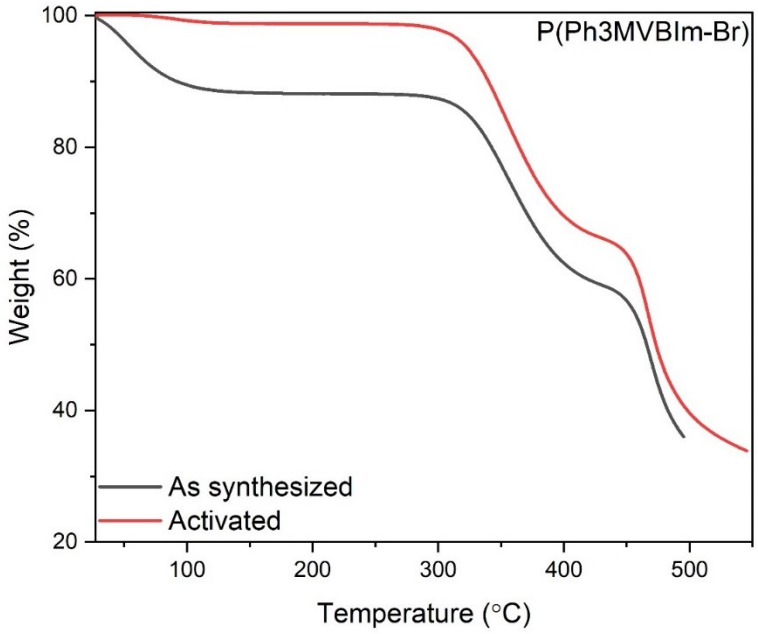

Figure S14: Thermogravimetric analysis profiles for polymer **P(Ph3MVBIm-Br)** as-synthesized (in black) and activated phase (in red).

X-ray Photoelectron Spectroscopy (XPS).

XPS was performed with a Kratos AXIS 165 spectrometer using monochromatic Al Kα radiation (1486.6 eV). High-resolution scans of specific elements, *i.e.*, C 1s, N 1s, and Br 3d, were recorded at pass energy of 20 eV while pass energy of 100 eV was used for the survey spectrum. The sample surface was saturated with low-energy electrons to neutralize the surface charge. Peak intensities were

evaluated by subtracting a Shirley-type background while considering the Scofield factor. Binding energies were calculated using the C 1s peak at the binding energy (BE) of 284.8 eV as a reference.

Table S2: Element contents of **P(Ph3MVBIm-Br)** obtained from XPS high resolution spectra:

Element	Position[a]	FWHM[b]	R.S.F[c]	Area	% Concentration
C 1s	284.7	2.4	1	61428	82.1
N 1s	401.3	1.4	1.8	16076	11.9
Br 3d	67.4	2.2	2.84	7835	3.7

a = position is binding energy (BE in eV).

b = FWHM is full width at half maximum of peak

c = RSF is relative sensitivity factor.

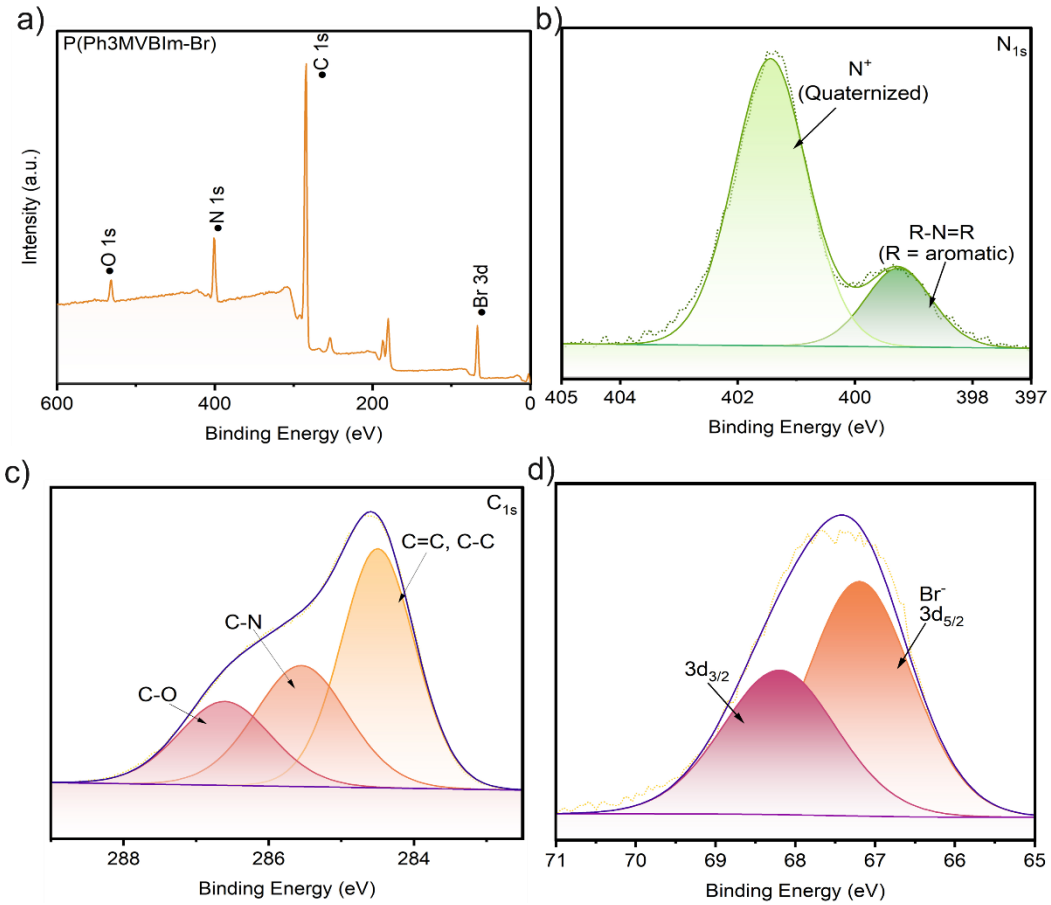

Figure S15: XPS analysis of **P(Ph3MVBIm-Br);** a) survey of the elements, the high-resolution data; b) for nitrogen; c). for carbon; d) for bromide.

Adsorption selectivity calculations.

The selectivities for the adsorbate mixture composition of interest were calculated from the single component adsorption isotherms using Ideal Adsorbed Solution Theory (IAST), using IAST++ program. First, the single-component isotherms for the gas sorbates at 298 K were fitted to the dual-site Langmuir-Freundlich (DSLF) equation.

$$q = q_A \frac{b_A\, pv^A}{1 + b_A pv^A} + q_A \frac{b_B\, pv^B}{1 + b_B pv^B}$$

Here, p is the pressure of the bulk gas at equilibrium with the adsorbed phase (Pa), q is the adsorbed amount per mass of adsorbent (mol.kg^{-1}), q_A an q_A are the saturation capacities of site A and B (mol/kg), b_A and b_B are the affinity coefficients of site A and B (Pa^{-1}), v^A and v^B represent the deviations from an ideal homogeneous surface.

The selectivity for C_2H_2/CO_2 separation was calculated using the following equation:

$$S_{ads} = \frac{\frac{q_1}{q_2}}{\frac{p_1}{p_2}}$$

where q_1 and q_2 are the molar loadings in the adsorbed phase in equilibrium with the bulk gas phasewith partial pressures p_1 and p_2.

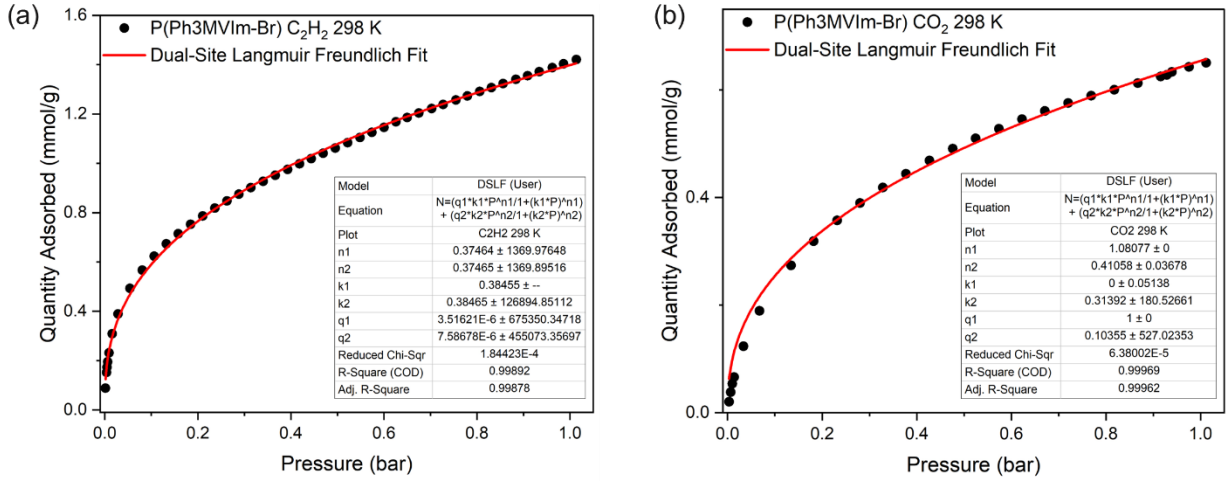

Figure S16: Fitting plots for adsorption isotherms of; a) C_2H_2 and b) CO_2 at 298 K for **P(Ph3MVIm-Br)** using Dual-site Langmuir model.

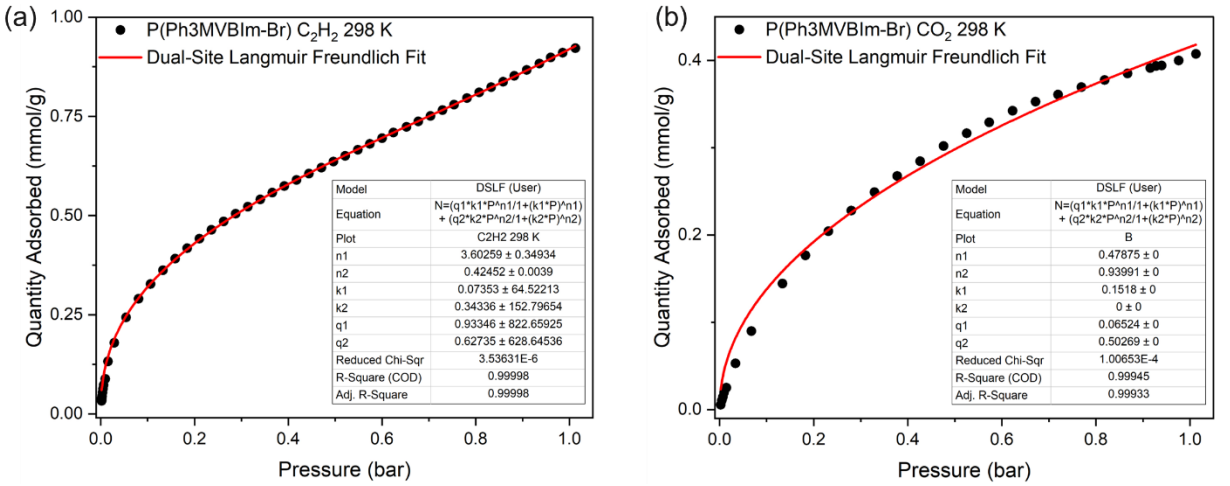

Figure S17: Fitting plots for adsorption isotherms of; a) C_2H_2 and b) CO_2 at 298 K for **P(Ph3MVBIm-Br)** using Dual-site Langmuir model.

Adsorption energy calculations.

Isosteric heat of adsorption (Q_{st}) values were calculated from isotherms measured at 273 K, 283 K and 298 K for C_2H_2 and CO_2. The isotherms were first fit to a viral equation:

$$lnP = lnN + \frac{1}{T}\sum_{i=0}^{mn} a_i N^i + \sum_{i=0}^{n} b_i N^i$$

Where *N* is the amount of gas adsorbed at the pressure *P*, *a* and *b* are virial coefficients, *m* and *n* are the number of coefficients require to adequately describe the isotherm. To calculate Q_{st}, the fitting parameters from the above equation were used for the following equation:

$$Q_{st} = -R\sum_{i=0}^{mn} a_i N^i$$

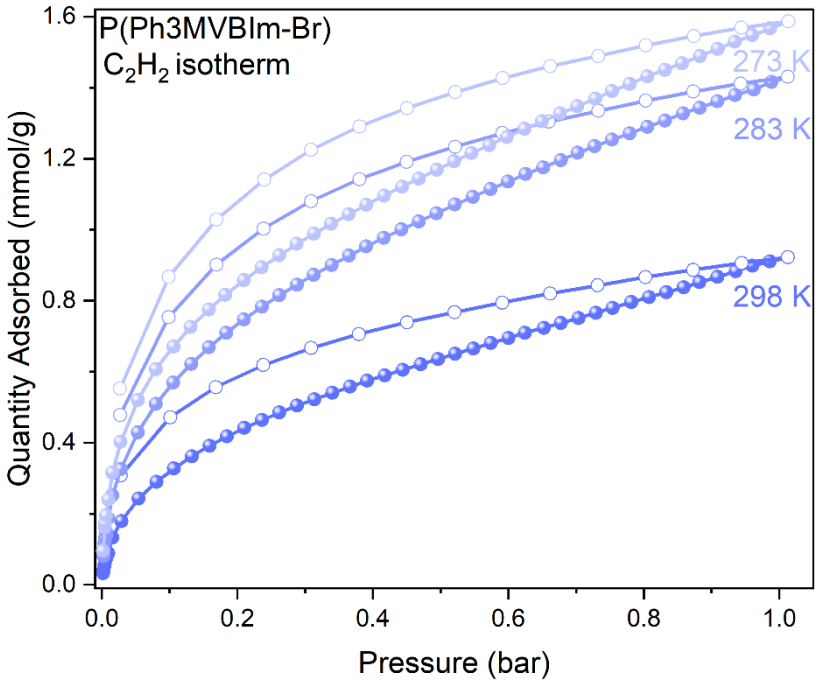

Figure S18: C_2H_2 isotherms recorded at 298 K, 283 K and 273 K, considered for Q_{st} determination (closed and open symbols denote adsorption and desorption, respectively).

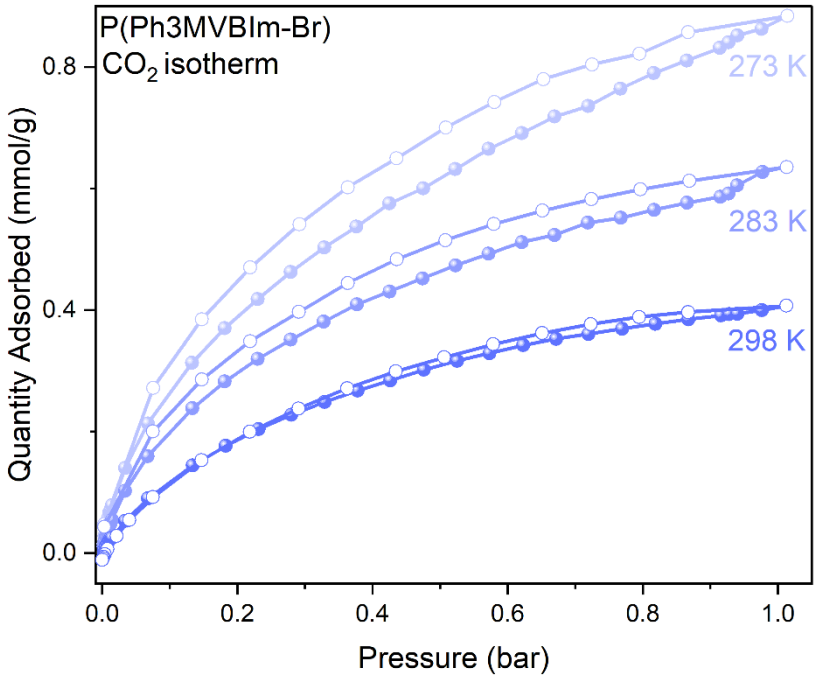

Figure S19: CO_2 isotherms recorded at 298 K, 283 K and 273 K, considered for Q_{st} determination (closed and open symbols denote adsorption and desorption, respectively).

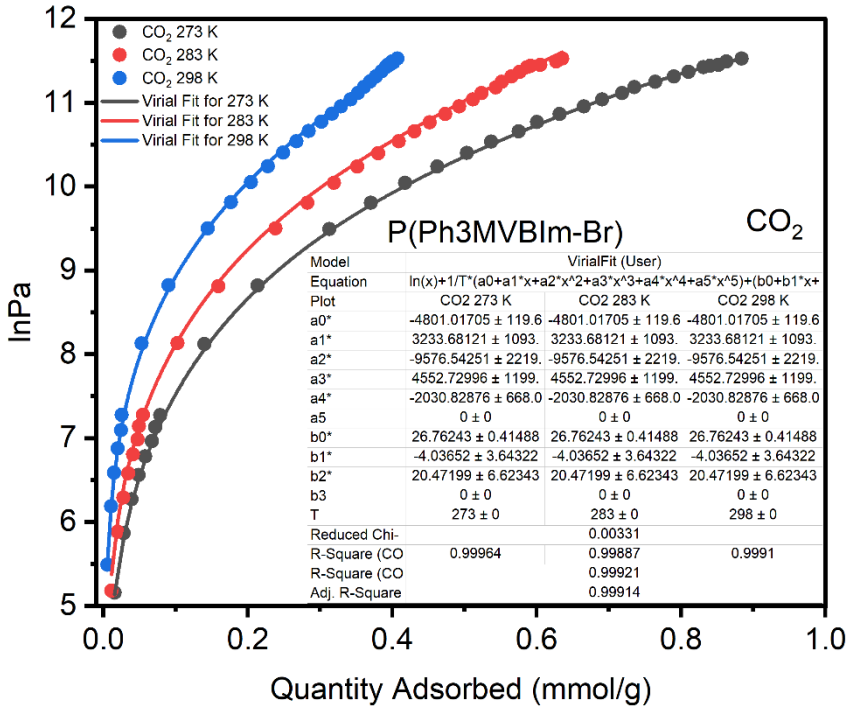

Model	VirialFit (User)		
Equation	ln(x)+1/T*(a0+a1*x+a2*x^2+a3*x^3+a4*x^4+a5*x^5)+(b0+b1*x+		
Plot	CO2 273 K	CO2 283 K	CO2 298 K
a0*	-4801.01705 ± 119.6	-4801.01705 ± 119.6	-4801.01705 ± 119.6
a1*	3233.68121 ± 1093.	3233.68121 ± 1093.	3233.68121 ± 1093.
a2*	-9576.54251 ± 2219.	-9576.54251 ± 2219.	-9576.54251 ± 2219.
a3*	4552.72996 ± 1199.	4552.72996 ± 1199.	4552.72996 ± 1199.
a4*	-2030.82876 ± 668.0	-2030.82876 ± 668.0	-2030.82876 ± 668.0
a5	0 ± 0	0 ± 0	0 ± 0
b0*	26.76243 ± 0.41488	26.76243 ± 0.41488	26.76243 ± 0.41488
b1*	-4.03652 ± 3.64322	-4.03652 ± 3.64322	-4.03652 ± 3.64322
b2*	20.47199 ± 6.62343	20.47199 ± 6.62343	20.47199 ± 6.62343
b3	0 ± 0	0 ± 0	0 ± 0
T	273 ± 0	283 ± 0	298 ± 0
Reduced Chi-		0.00331	
R-Square (CO	0.99964	0.99887	0.9991
R-Square (CO		0.99921	
Adj. R-Square		0.99914	

Figure S20: Virial fit on CO_2 adsorption isotherms at three different temperatures.

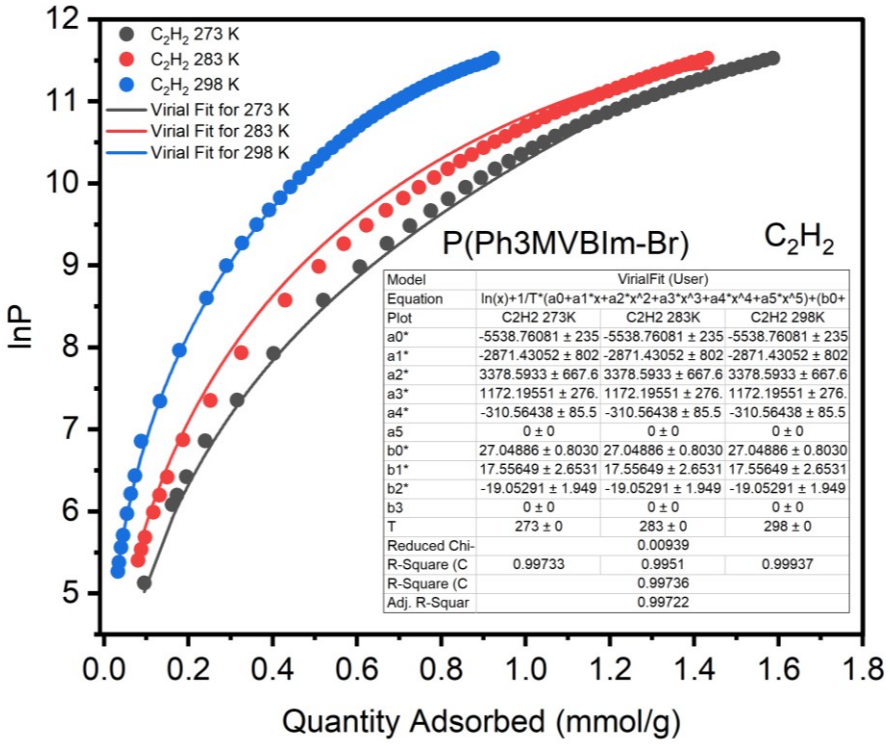

Model	VirialFit (User)		
Equation	ln(x)+1/T*(a0+a1*x+a2*x^2+a3*x^3+a4*x^4+a5*x^5)+(b0+		
Plot	C2H2 273K	C2H2 283K	C2H2 298K
a0*	-5538.76081 ± 235	-5538.76081 ± 235	-5538.76081 ± 235
a1*	-2871.43052 ± 802	-2871.43052 ± 802	-2871.43052 ± 802
a2*	3378.5933 ± 667.6	3378.5933 ± 667.6	3378.5933 ± 667.6
a3*	1172.19551 ± 276.	1172.19551 ± 276.	1172.19551 ± 276.
a4*	-310.56438 ± 85.5	-310.56438 ± 85.5	-310.56438 ± 85.5
a5	0 ± 0	0 ± 0	0 ± 0
b0*	27.04886 ± 0.8030	27.04886 ± 0.8030	27.04886 ± 0.8030
b1*	17.55649 ± 2.6531	17.55649 ± 2.6531	17.55649 ± 2.6531
b2*	-19.05291 ± 1.949	-19.05291 ± 1.949	-19.05291 ± 1.949
b3	0 ± 0	0 ± 0	0 ± 0
T	273 ± 0	283 ± 0	298 ± 0
Reduced Chi-		0.00939	
R-Square (C	0.99733	0.9951	0.99937
R-Square (C		0.99736	
Adj. R-Squar		0.99722	

Figure S21: Virial fit on C_2H_2 adsorption isotherms at three different temperatures. Pressure on Y axis is in Pascal.

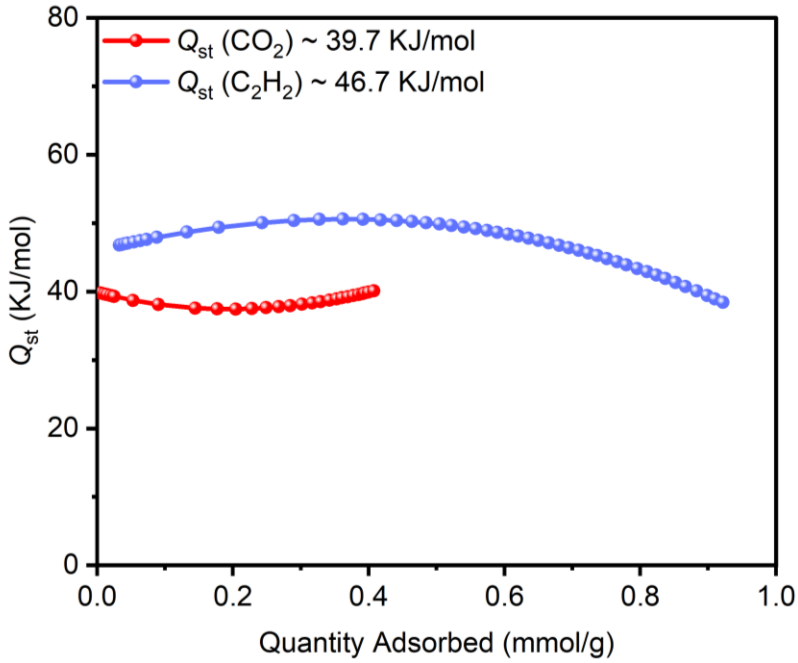

Figure S22: Adsorption enthalpy (Q_{st}) of C_2H_2 and CO_2 for **P(Ph3MVBIm-Br)**.

Table S4: Summary of the adsorption uptake (298 K), uptake ratio, selectivity, and heat of adsorption for several top-performing C_2H_2/CO_2 separating organic physisorbents.

Sample	Uptake ratio	IAST Selectivity (1:1)	Q_{st} of C_2H_2 (kJ/mol)	Reference
P(Ph3MVIm-Br)	1.55	4.9	-	This work
P(Ph3MVBIm-Br)	2.27	8.5	46.73	This work
P(Ph3Im-Br-0.5DVB)	2.51	17.9	40.9	[11]
P(Ph3Im-Br-DVB)	2.06	8.3	-	[11]
2D sql COF	1.97	4.8	45	[12]
3D pts COF	2.23	3.8	14.4	[12]
NKCOF-12	1.42	4.0	32	[13]
ZJUT-2	1.74	3.1	31.9	[14]
ZJUT-3	2.16	3.2	26.7	[14]
NUS-71	4.12	16	32.7	[15]
NUS-72	4.29	6.7	30.1	[15]
HOF-3a	2.23	21	19	[16]
ECUT-HOF-30a	4.86	9	23.8	[17]
CPOC-101α	1.5	11.9	23.5	[18]

Dynamic column breakthrough experiments.

Based on single-component gas sorption data, we conducted dynamic column breakthrough (DCB) experiments on a sample of **P(Ph3MVBIm-Br)**. A 1:1 C_2H_2/CO_2 mixture was passed through a column packed with the activated sample at a total flow rate of 1.0 cm^3/min, with the effluent composition monitored via mass spectrometry.

Temperature-programmed desorption (TPD) experiments were performed following the adsorption branches of the DCB experiments for **P(Ph3MVBIm-Br)**. The inlet gas mixture was replaced with 20 cm^3/min of He, and a temperature ramp of 5 °C min^{-1} was applied from 25 °C to 60 °C. Desorption was continued until no further adsorbate was detected.

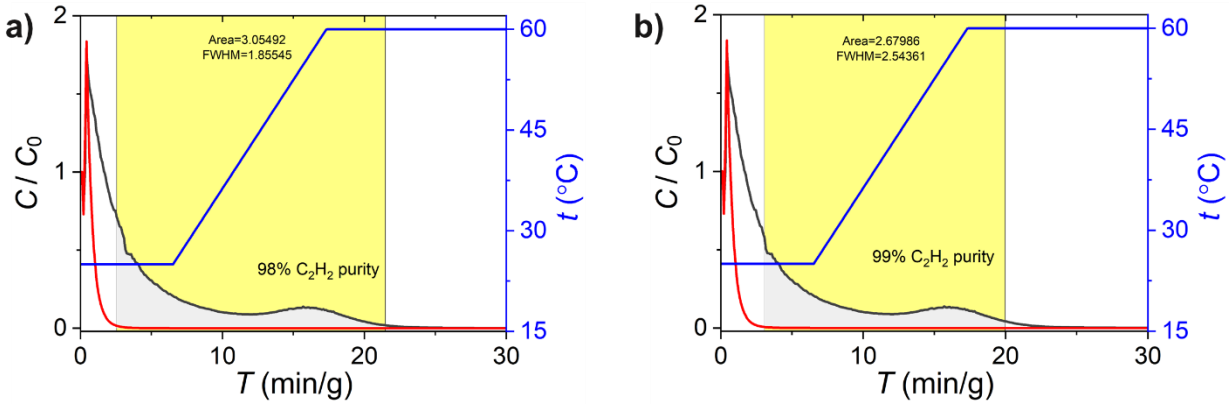

Figure S23: TPD plots for **P(Ph3MVBIm-Br)**; a) Fuel-grade C_2H_2 elution, b) High-purity laboratory grade C_2H_2 elution.

Crystallographic data.

Table S5: Crystallographic data and structure refinement details for **Ph3MVIm-Br**.

3,3',3''-(benzene-1,3,5 triyltris(methylene))tris(1-vinyl-1*H*-imidazol-3-ium) [**Ph3MVIm-Br**]	
CCDC number	2418964
Formula	$C_{24}H_{27}N_6Br_3(H_2O)_2$
Formula weight	675.28
Temperature (K)	159(2)
Crystal system	Triclinic
Space group	*P*-1
a(Å)	7.1766(3)
b(Å)	11.8425(4)
c(Å)	16.5364(6)
α(°)	84.628(2)
β(°)	87.323(2)
γ(°)	81.602(2)
V (Å^3)	1383.46(9)
D_c (g/cm $^{-3}$)	1.621
μ(mm^{-1})	5.670
F(000)	676
Crystal size (mm^3)	0.20 x 0.20 x 0.20
Reflections collected/unique	55348/4871 [R(int) = 0.0734]
Completeness (%)	99.6
Reflections with [$I>2\sigma(I)$]	4218
Data / restraints / parameters	4871 / 10 / 359
GOF on F^2	1.005
R_1, wR_2 [$I>2\sigma(I)$]	0.0342, 0.0869
R_1, wR_2 (all data)	0.0410, 0.0911

Computational studies.

Accelerated molecular dynamics (MD) simulations were performed to model the polymerization process until an ionic ultramicroporous polymer (IUP) model system was formed. Subsequently, canonical Monte Carlo (MC) simulations were conducted to identify the most plausible adsorption binding sites. All simulations were carried out using the Materials Studio platform.[19] The specific methodologies and parameters for each simulation are described in detail below.

Pre-polymerization

Initially, the **Ph3MVIm-Br** and **Ph3MVBIm-Br** monomers were optimized using the Conjugate Gradient method. The third version of the Condensed-phase Optimized Molecular Potentials for Atomistic Simulation Studies (COMPASS-III)[19,20] from the Materials Studio[19] forcefield library was employed to calculate intramolecular and intermolecular bonded and non-bonded forces in the systems. Atomic point charges for the monomers were also assigned using the COMPASS III forcefield. **Fig. S24** illustrates the molecular structures of the optimized monomers.

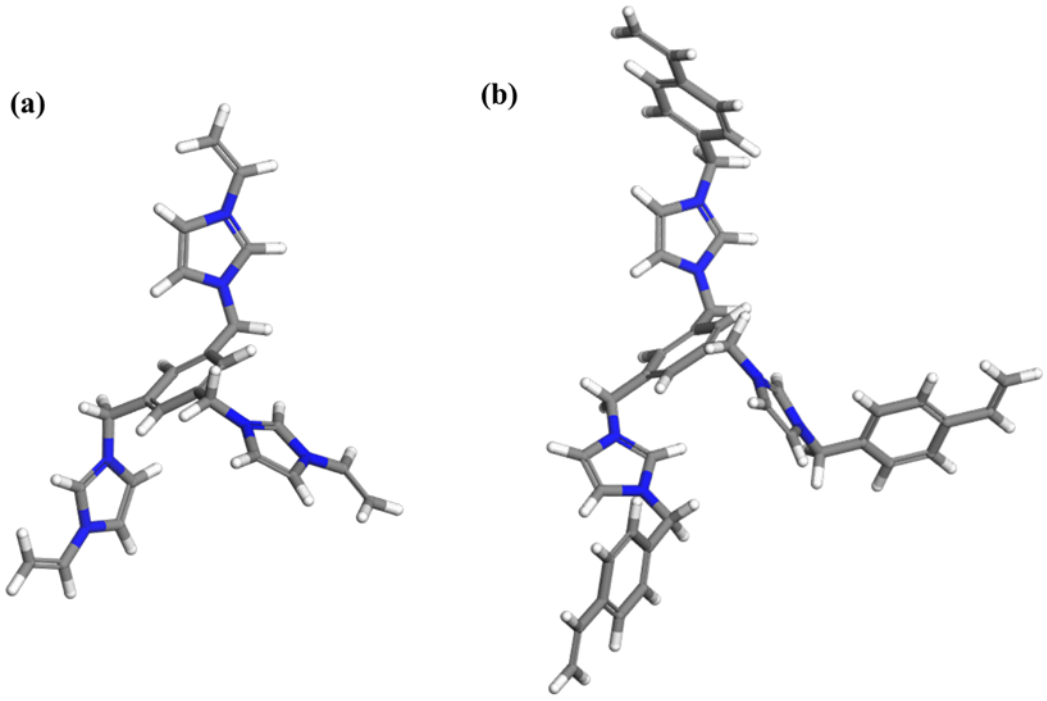

Figure S24: Optimized structures of (a) **Ph3MVIm-Br**, and (b) **Ph3MVBIm-Br**. Carbon, nitrogen, and hydrogen atoms are presented in grey, blue, and white, respectively.

To model the radical polymerization reaction of the monomers, we adopted the following assumptions:

1. The initiation reaction proceeds to full conversion (100%), meaning the concentration of the free radicals generated during initiation is equal to the initial concentration of the initiator (AIBN).
2. During the initiation reaction, all three arms of the reacted monomer are assumed to form free radicals, as shown in **Scheme S1** and **Fig. S25**, with the reactive sites labelled as R*.

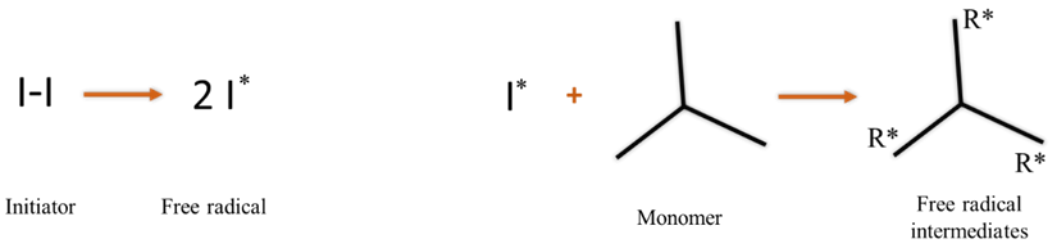

Scheme S1: Radical initiation and free radical intermediate formation.

3. For each monomer, a simulation box of 70 × 70 × 70 Å³ was constructed, containing monomers, free radicals, water molecules, ethanol, and toluene, based on the experimental concentrations (mentioned earlier in synthesis section). Both systems were neutralized by adding bromide ions (Br^-). The number of molecules for each component and the initial pre-propagation models are provided in **Table S6** and **Fig. S26**, respectively.

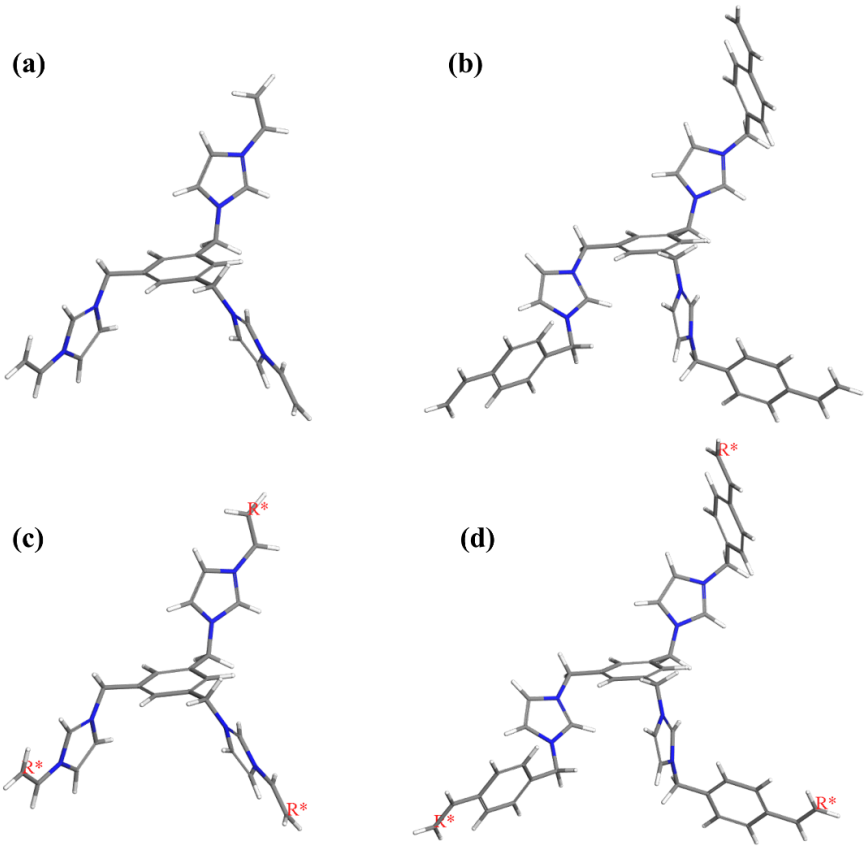

Figure S25: Pre-defined repeat units of (a) **Ph3MVIm-Br**, and (b) **Ph3MVBIm-Br**. Free radical intermediates formed during the initiation step of the polymerization process, with reactive sites or the monomers labelled as R* for (c) **Ph3MVIm-Br**, and (d) **Ph3MVBIm-Br**.

vid

Table S6: Concentration of the system's initial components in a 70 × 70 × 70 Å^3 simulation box.

Components	Mol-%	Number of molecules
Monomer	0.7834	41
Initiator	0.2325	12*
Water	44.2028	2293
Ethanol	54.7758	2841
Toluene	0.0055	0

* The number of free radical intermediates is the $\frac{\text{number of initiator molecules}}{3}$ = 4

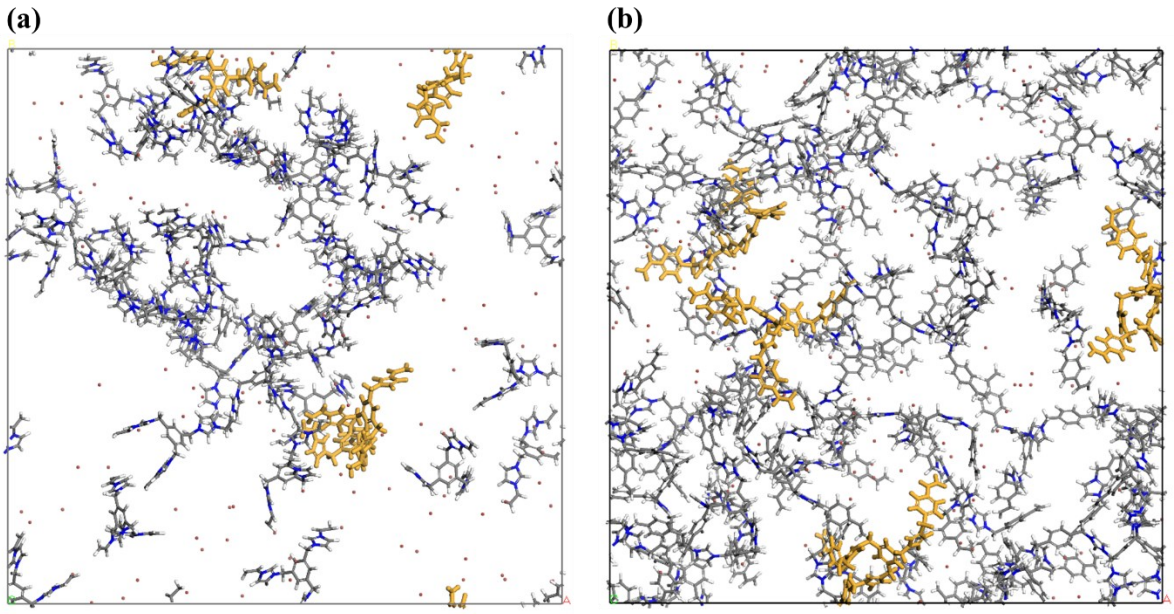

Figure S26: The pre-propagation models of the systems include (a) **Ph3MVIm-Br**, and (b) **Ph3MVBIm-Br** monomers. The free radical intermediates are shown in orange. The brown balls represent Br^- ions. For clarity, the solvent molecules (water, and ethanol) are not shown.

Polymerization step

For the propagation simulation (polymerization simulation), a Perl script was developed within the Materials Studio platform, inspired by the Polymatic algorithm.[21] The Polymatic algorithm can be used to describe reactive polymerization in LAMMPS.[22] The COMPASS III forcefield was used to calculate intramolecular and intermolecular bonded and non-bonded forces throughout the polymerization process and in the final structures. The polymerization steps proceed as follows (see **Fig. S27** for a flowchart of the applied polymerization algorithm):

1. The nearest reactive atom pair that meets the bonding criteria is identified.
2. A bond is formed, followed by energy minimization of the structure and removing any artificial charges.
3. Steps (1) and (2) continue until no suitable reactive pair is identified.

4. If no suitable reactive pair is identified, MD simulations are conducted to bring the remaining reactive pairs into closer proximity within the system, marking the end of a polymerization cycle
5. The algorithm is executed for a maximum of 50 polymerization cycles (N_{max} = 50), with all possible bond formations occurring in each cycle, followed by energy minimization and bond relaxation.

Artificial charges with a value of ±e were applied during polymerization to accelerate bonding by assigning opposite charges to reactive atoms, promoting their interaction during molecular dynamics while maintaining overall charge neutrality. These charges were removed immediately after bond formation to avoid impacting the final polymer structure.

In each cycle, all possible polymerization steps (steps (1) and (2)) are executed. After each bond formation (see the one-bond formation scheme for both monomers in **Fig. S28** and **S29**), artificial charges are removed, followed by energy minimization and an MD NVT simulation to relieve residual stresses and enable structural rearrangement (see **Table S7** for details). Energy minimization relaxes the newly formed bonds, while MD ensures deeper structural relaxation and allows for structural fluctuations. These steps are applied in the code after each bond formation to rapidly adjust bond lengths and stabilize the structure.

If no reactive pairs are identified, the system undergoes MD NVT and MD NPT simulations (see **Table S7** for details). The cycles continue until no reactive pairs satisfy the bonding criteria. Finally, all remaining artificial charges are removed, and unsaturated polymer chain endpoints are saturated by adding hydrogen atoms (see **Table S7** for details).

Table S7: Energy minimization and MD simulation details during polymerization process.

Steps	Energy minimization (Geometry optimization)	MD NVT	MD NPT
After bond formation	Steepest descent algorithm	Simulation time = 25 ps Simulation time step = 0.5 to 1 fs Temperature = 298 K	N/A
If no pair reactive is found	N/A	Simulation time = 100 ps Simulation time step = 1 fs Temperature = 298 - 500 K	Simulation time = 100 ps Simulation time step = 1 fs Temperature = 298 - 500 K Pressure = 1 to 5 bar

Post-polymerization step

After the polymerization step, NVT and NPT simulations were conducted to equilibrate the final polymers, each for 10 ns with a time step of 1 fs at a temperature of 298 K and pressure of 1 bar. Following this, akin to the experimental washing step, all solvent molecules were removed from the simulation boxes. The polymer chains and Br^- ions were then equilibrated using NPT 10 ns simulation at 298 K and 1 bar.

During the NVT and NPT MD simulations, both during and after polymerization, temperature, and pressure were controlled using a Nosé-Hoover thermostat and a Berendsen barostat. Atomic positions

of the adsorbates were updated using the velocity Verlet algorithm with a cutoff distance of 12.5 Å, and long-range interactions were calculated using the Ewald method.[23]

A key aspect of the simulated polymerization algorithm is defining a 'polymerization step,' with repeat units pre-defined as in the final polymer structure (see **Fig. S24**). This avoids adding or removing atoms, requiring only updates to bonded interaction terms (*e.g.*, bond, angle, dihedral). Reactive atoms are identified by unique atom types, ensuring correct polymer structure rather than replicating the synthesis process. Since chemical reactions are not explicitly modelled in classical simulations, bonding criteria are applied to prevent unrealistic structures and excessive stress during bond formation, which energy minimization and MD simulations may not fully relax. In this study, a cutoff radius ranging from 4 to 10 Å was used for bond formation, with larger values applied near the end of polymerization to ensure

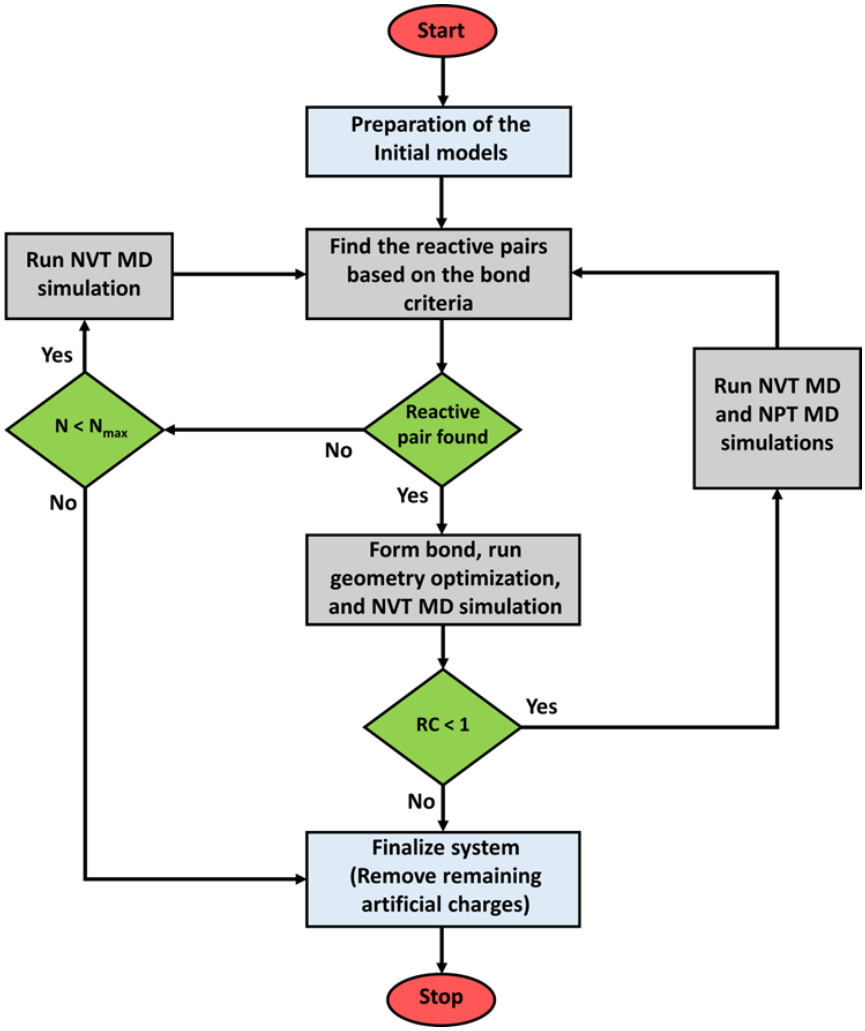

Figure S27: Flowchart illustrating the polymerization algorithm. Here, N represents the current number of polymerization cycles, N_{max} is the maximum allowed cycles, and RC denotes the reaction conversion (RC = $\frac{N_0 - N_t}{N_0}$, N_0 is initial number of monomer molecules and N_t is Number of monomer molecules at time t.

completion. The polymerization process versus time for both monomers is shown in Supporting Videos, **Ph3MVIm-Br.mp4** and **Ph3MVBIm-Br.mp4**. The final polymer structures are shown in **Fig. S30**. Both polymers show a particle-like morphology. The density of the internal structure was determined by calculating the volume and mass of each polymer particle, followed by averaging to obtain the final

densities, as presented in **Table S8**. The results indicate that **P(Ph3MVIm-Br)** has a higher density than **P(Ph3MVBIm-Br)**, which can be attributed to the longer arms of **Ph3MVBIm-Br**. These longer arms introduce more free volume within the polymer particles, resulting in a lower overall density. The simulation results are quite consistent with experimental findings (see **Table S8**). However, we remark the agreement could even have been better for the spherical **P(Ph3MVIm-Br)** model (**Figure S30**a) by considering NPT-MD equilibration of larger supercell models, which would automatically account for packing effects and lead to a higher density of the simulated model.

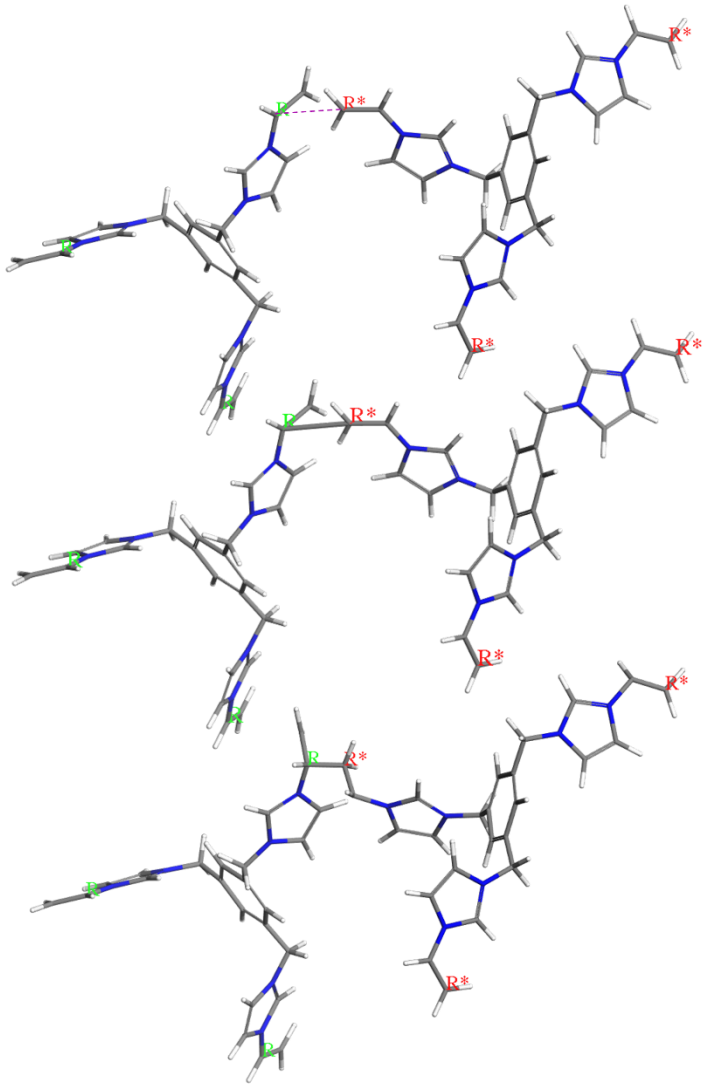

Figure S28: One-bond polymerization step is illustrated for **Ph3MVIm-Br**, in which the initial free radical bonds to a monomer. The radical sites and reactive sites as they assigned before coupling are shown with red R* and green R, respectively. Note that after the C-C coupling process between R and R*, carbon atom with the propagating radical is assigned as R*, whereafter the polymerization algorithm (**Figure S27**) continues.

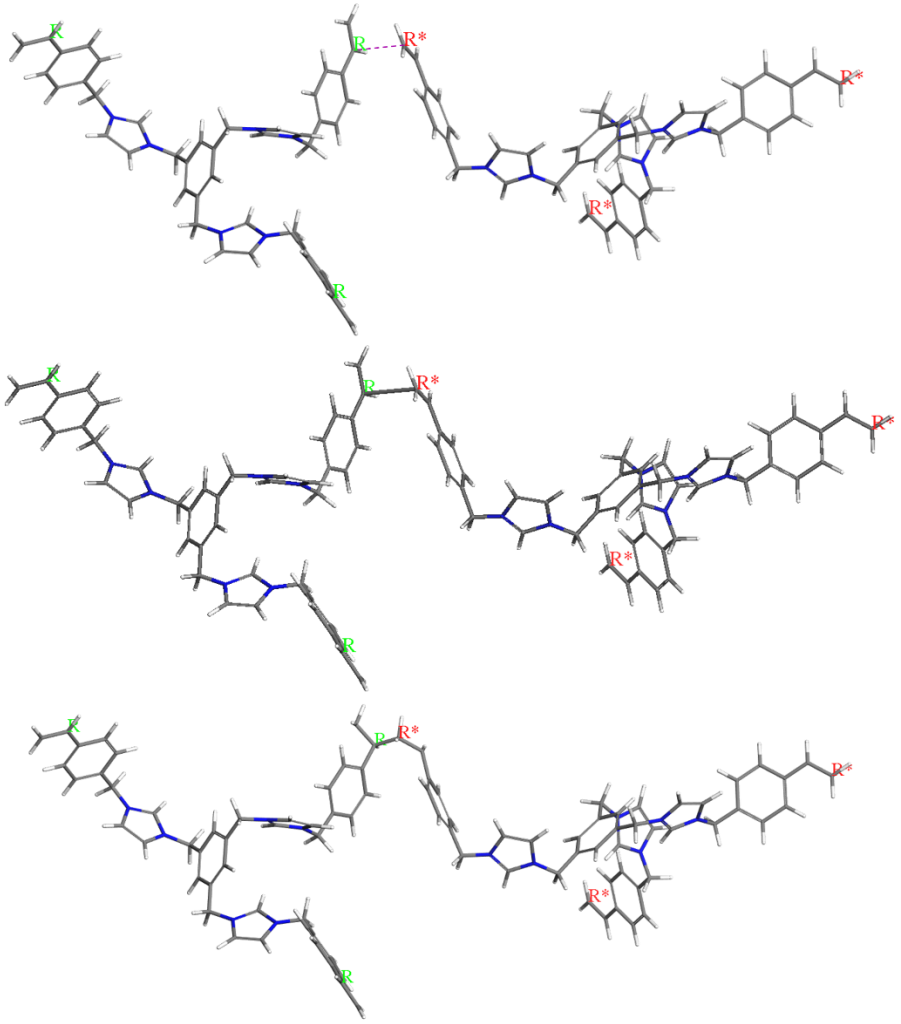

Figure S29: One-bond polymerization step is illustrated for **Ph3MVBIm-Br**, in which the initial free radical bonds to a monomer. The radical sites and reactive sites as they assigned before coupling are shown with red R* and green R, respectively.

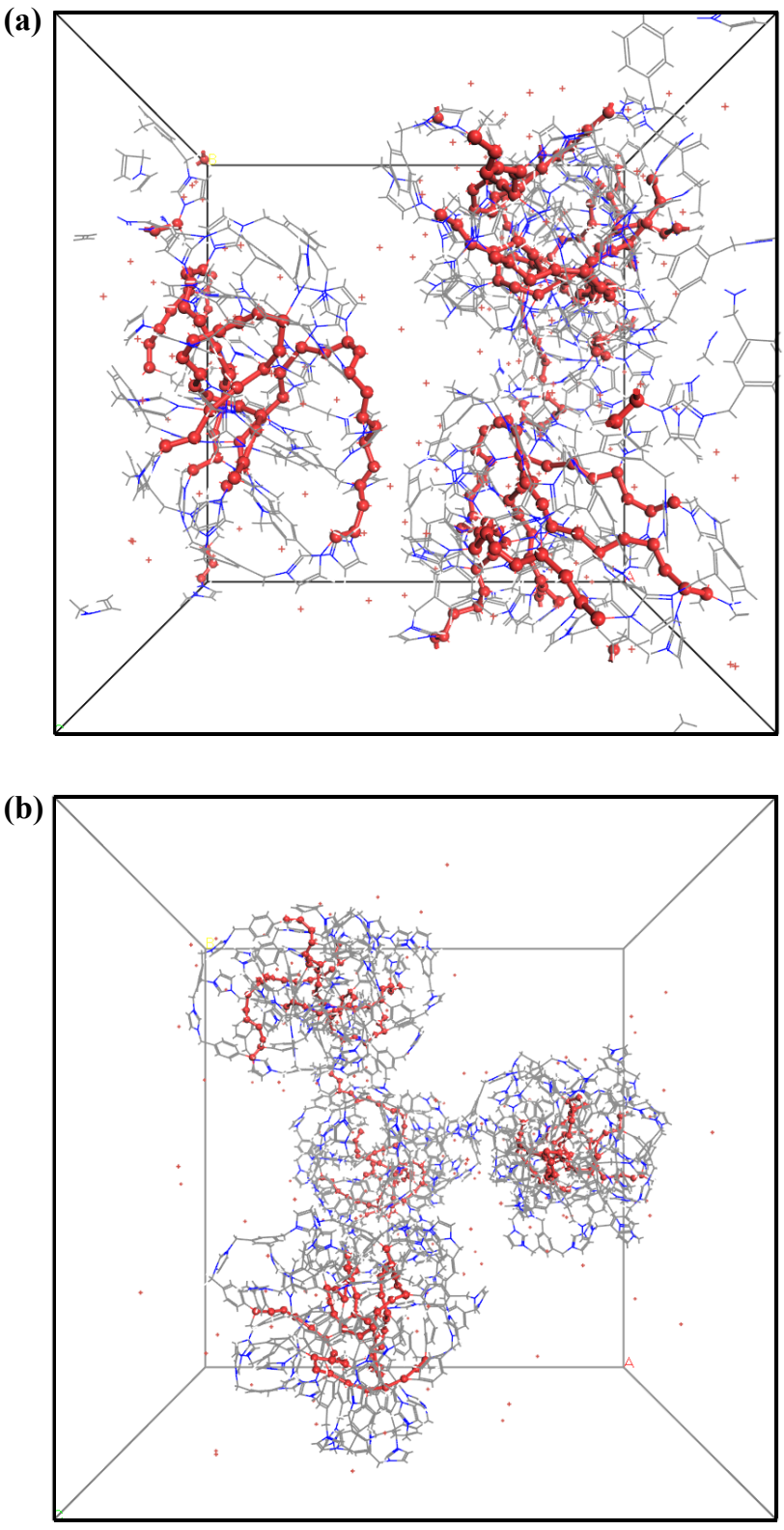

Figure S30: The final structures of (a) **P(Ph3MVIm-Br)** and (b) **P(Ph3MVBIm-Br)** obtained from the polymerization simulation. Newly formed bonds are depicted in red using a ball-and-stick representation, while Br^- ions are shown as brown dots.

Table S8. Density of the polymers produced through polymerization simulations, with the standard deviation calculated from the average particle densities.

Polymer	Simulated density (g/cm^3)	Experimental density* (g/cm^3)
P(Ph3MVIm-Br)	1.65 ± 0.02	2.11 ± 0.03
P(Ph3MVBIm-Br)	1.60 ± 0.04	1.58 ± 0.0083

*Data recorded using Anton Paar Ultrapyc 5000 gas pycnometer with nitrogen gas as probe at 20 °C.

Canonical Monte Carlo (CMC) simulations[24] were performed to confirm the main binding site locations for C_2H_2 and CO_2 in **P(Ph3MVIm-Br)** and **P(Ph3MVBIm-Br)**. CMC simulations were performed in Materials Studio at 298 K on the final structure of the polymers. To describe the electrostatics upon adsorption, the atomic point charges of the polymers and the adsorbates were determined via COMPASS III forcefield. The point charges used for C_2H_2 and CO_2 are given in **Fig. S31**. Furthermore, the bonded and non-bonded interactions in the systems were calculated using COMPASS III forcefield from the Material Studio forcefield library. A cut-off distance of 12.5 Å was applied for non-bonded interactions, with the potentials smoothly truncated using a cubic spline function over a spline width of 1 Å. Electrostatic interactions were calculated using the Ewald summation method[25] for enhanced accuracy.

For the CMC simulations, the polymers were considered rigid, with atoms fixed at their post-polymerization optimized positions and a fixed loading of 30 adsorbate molecules. In the canonical ensemble, the Metropolis sampling method considered different moves, such as translation (corresponds with a translation of the selected adsorbate molecule), rotation around the centre of mass of the selected adsorbate molecule, regrowth (removes a selected adsorbate molecule from the system and reintroduces it at a random position with random orientation), and conformer (collects multiple adsorbate conformations), with relative probabilities of 1, 1, 0.1 and 1, respectively.

CMC simulations included 3×10^6 loading steps, followed by 3×10^6 equilibration steps, and finally, 3×10^6 production steps to ensure reasonable ensemble averages. The output of the CMC simulations was visualized as adsorbate density fields, encompassing the mass-middle points of all successful adsorbate MC moves (see **Figures S32** and **S33**). The density field analysis provides valuable insights into the adsorption behaviour of the studied polymers. The results indicate that the adsorption binding sites are primarily located on the surface of the polymer particles rather than inside them. This finding highlights that surface adsorption is the dominant mechanism for C_2H_2 and CO_2 in both **P(Ph3MVIm-Br)** and **P(Ph3MVBIm-Br)**. The particle morphology of **P(Ph3MVIm-Br)** and **P(Ph3MVBIm-Br)**, with high densities (see **Table S8**), influences the adsorption mechanism. Observations from the simulations reveal that Br^- ions predominantly reside on the polymer particles' surface (see **Fig. S30**), forming a shielding layer. This layer not only creates a highly electronegative environment that strongly interacts with polarizable gas molecules such as CO_2 and C_2H_2 but also acts as a barrier, limiting gas diffusion into the dense polymer interior. Consequently, surface adsorption emerges as the dominant mechanism,

driven by the interplay of electrostatic interactions, steric hindrance from bulky phenyl groups, and the compact internal structure of the polymers.

We also created an isosurface of constant density and coloured it by the potential energy (see **Fig. 3** in the main text). From the colour-mapped isosurfaces, it can be observed both C_2H_2 and CO_2 have more affinity for **P(Ph3MVIm-Br)**. The denser packing of functional groups in **P(Ph3MVIm-Br)** could increase the probability of gas molecules interacting with multiple adsorption sites simultaneously, potentially reinforcing adsorption. Depending on the dominant adsorption mechanism, this effect may occur both within the polymer structure and on its surface. Our computational results indicate that surface adsorption plays a primary role in both polymers. Given this, the more compact structure of **P(Ph3MVIm-Br)** may enhance both surface and internal adsorption, further contributing to its higher gas uptake.

This compact framework may also contribute to a higher binding site density, which could lead to greater overall gas uptake. Additionally, the well-organized structure might promote more efficient molecular confinement, possibly improving C_2H_2 selectivity due to its higher quadrupole moment.

P(Ph3MBIm-Br), on the other hand, has a looser structure due to the presence of benzyl groups, which introduce additional free volume within the polymer. This expanded framework may result in a more widely distributed arrangement of functional sites, reducing the likelihood of strong cooperative interactions between adsorbed gas molecules and the polymer matrix. Consequently, gas-polymer interactions could be weaker at 298 K, which potentially leads to lower adsorption efficiency and selectivity.

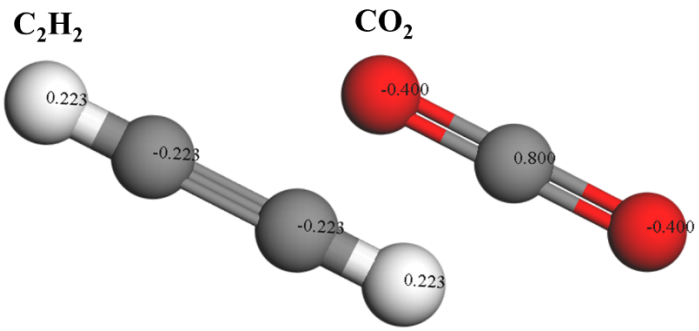

Figure S31: Atomic structures and point charges of C_2H_2 and CO_2.

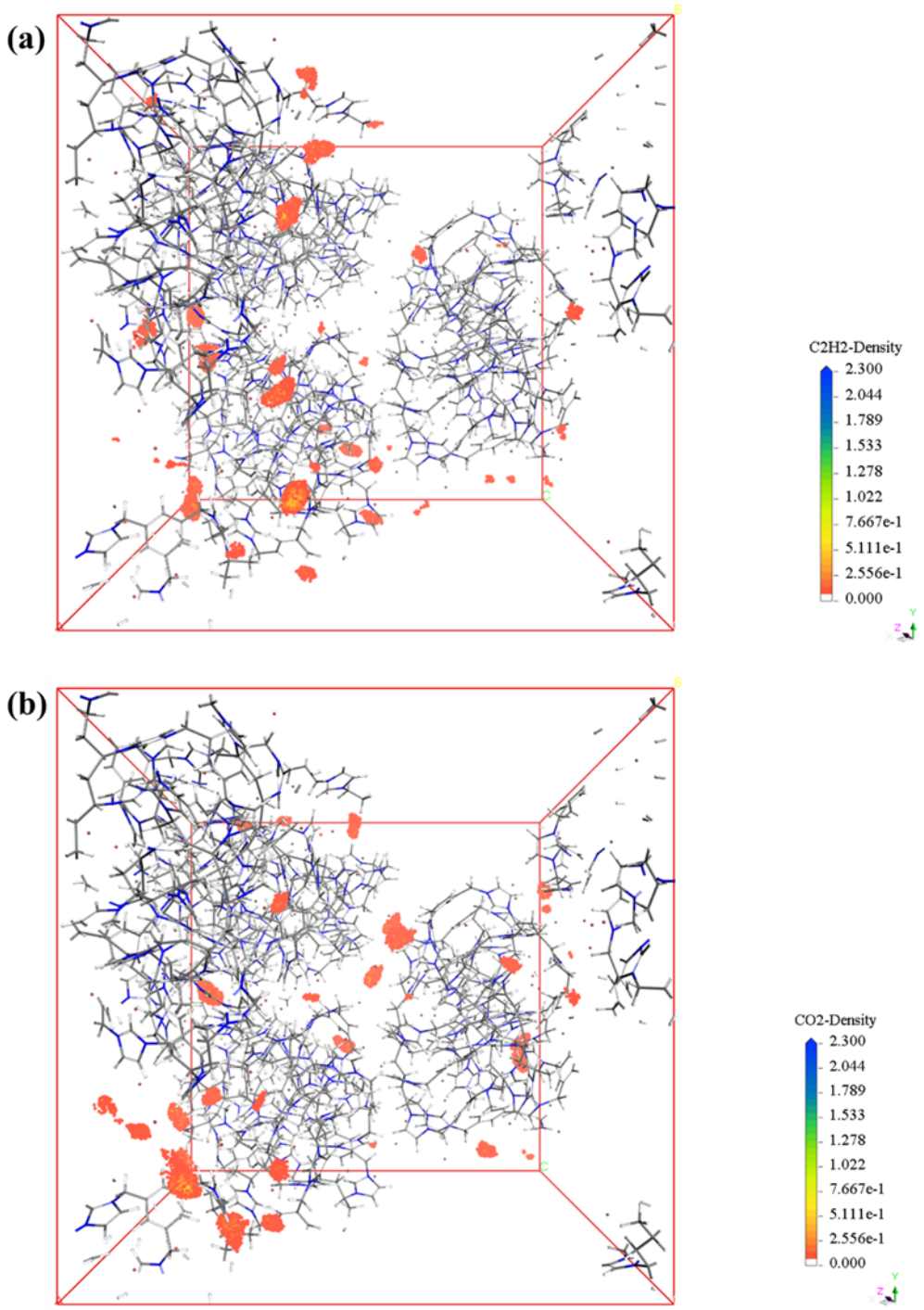

Figure S32: The adsorbate density fields obtained from CMC simulations for (a) C_2H_2 and (b) CO_2, at 298 K in **P(Ph3MVIm-Br)**. They allow the identification of optimal binding sites. The colour map values indicate the density of the adsorbate in molecules/Å^3.

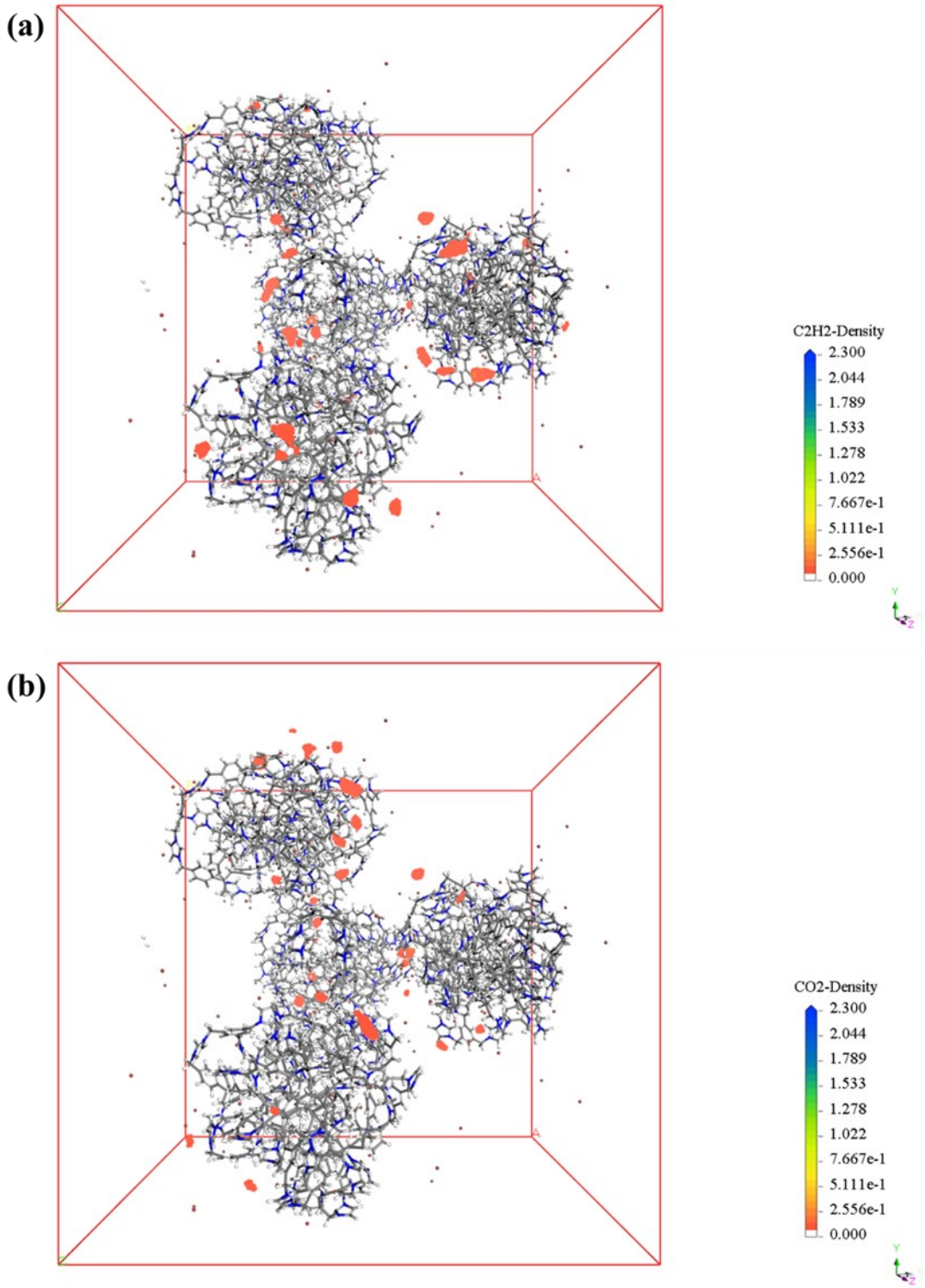

Figure S33: The adsorbate density fields obtained from CMC simulations for (a) C_2H_2 and (b) CO_2, at 298 K in **P(Ph3MVBIm-Br)**. They allow the identification of optimal binding sites. The colour map values indicate the density of the adsorbate in molecules/Å^3.

References.

1 J.-F. Soulé, H. Miyamura and S. Kobayashi, *J. Am. Chem. Soc.*, 2013, **135**, 10602–10605.

2 A. García-Valenzuela, M. Butterling, M. O. Liedke, E. Hirschmann, T. T. Trinh, A. G. Attallah, A. Wagner, R. Alvarez, J. Gil-Rostra, V. Rico, A. Palmero and A. R. González-Elipe, *Microporous Mesoporous Mater.*, 2020, **295**, 109968.

3 T. Goworek, *Annales UMCS, Chemia*, 2015, **69**, 1–110.

4 G. Dlubek, S. Eichler, Ch. Hübner and Ch. Nagel, *Phys. Status Solidi A*, 1999, **174**, 313–325.

5 T. L. Dull, W. E. Frieze, D. W. Gidley, J. N. Sun and A. F. Yee, *J. Phys. Chem. B*, 2001, **105**, 4657–4662.

6 M. Gorgol, M. Tydda, A. Kierys and R. Zaleski, *Microporous Mesoporous Mater.*, 2012, **163**, 276–281.

7 S. J. Tao, *J Chem Phys*, 1972, **56**, 5499–5510.

8 M. Eldrup, D. Lightbody and J. N. Sherwood, *Chem Phys.*, 1981, **63**, 51–58.

9 T. Goworek, K. Ciesielski, B. Jasińska and J. Wawryszczuk, *Chem. Phys. Lett.*, 1997, **272**, 91–95.

10 J. V. Olsen, P. Kirkegaard, N. J. Pedersen and M. Eldrup, in *Physica Status Solidi (C) Current Topics in Solid State Physics*, Wiley-VCH Verlag, 2007, **4**, 4004–4006.

11 H. Pan, X. Suo, Z. Yang, L. Yang, X. Cui and H. Xing, *Adv. Funct. Mater.*, 2023, **20**, 2214887.

12 L. Chen, C. Gong, X. Wang, F. Dai, M. Huang, X. Wu, C.-Z. Lu and Y. Peng, *J. Am. Chem. Soc.*, 2021, **143**, 10243–10249.

13 P. Zhang, Z. Wang, Y. Yang, S. Wang, T. Wang, J. Liu, P. Cheng, Y. Chen and Z. Zhang, *Sci. China Chem.*, 2022, **65**, 1173–1184.

14 C. Gong, H. Wang, G. Sheng, X. Wang, X. Xu, J. Wang, X. Miao, Y. Liu, Y. Zhang, F. Dai, L. Chen, N. Li, G. Xu, J. Jia, Y. Zhu and Y. Peng, *Angew. Chem. Int. Ed.,* 2022, **32**, e202204899.

15 Z. Zhang, C. Kang, S. B. Peh, D. Shi, F. Yang, Q. Liu and D. Zhao, *J. Am. Chem. Soc.*, 2022, **144**, 14992–14996.

16 P. Li, Y. He, Y. Zhao, L. Weng, H. Wang, R. Krishna, H. Wu, W. Zhou, M. O'Keeffe, Y. Han and B. Chen, *Angew. Chem. Int. Ed.*, 2015, **54**, 574–577.

17 L. Wang, L. Yang, L. Gong, R. Krishna, Z. Gao, Y. Tao, W. Yin, Z. Xu and F. Luo, *Chem. Eng. J.*, 2020, **383**, 123117.

18 W. Wang, K. Su, E.-S. M. El-Sayed, M. Yang and D. Yuan, *ACS Appl. Mater. Interfaces*, 2021, **13**, 24042–24050.

19 BIOVIA, Material Studio, San Diego: Dassault Systèmes, **2023**.

20 H. Sun, *J Phys. Chem. B*, 1998, **102**, 7338–7364.

21 L. J. Abbott, K. E. Hart and C. M. Colina, *Theor. Chem. Acc.*, 2013, **132**, 1334.

22 A. P. Thompson, H. M. Aktulga, R. Berger, D. S. Bolintineanu, W. M. Brown, P. S. Crozier, P. J. in 't Veld, A. Kohlmeyer, S. G. Moore, T. D. Nguyen, R. Shan, M. J. Stevens, J. Tranchida, C. Trott and S. J. Plimpton, *Comput. Phys. Commun.*, 2022, **271**, 108171.

23 A. Y. Toukmaji and J. A. Board, *Comput. Phys. Commun.*, 1996, **95**, 73–92.

24 D. Frenkel, B. Smit and M. A. Ratner, *Phys. Today*, 1997, **50**, 66–66.

25 A. Y. Toukmaji and J. A. Board, *Comput. Phys. Commun.*, 1996, **95**, 73–92.